https://doi.org/10.5194/egusphere-2026-6816
Preprint. Discussion started: 17 November 2026
© Author(s) 2026. CC BY 4.0 License.

# Assessment of the EarthCARE CPR spectral width retrieval: signal-level simulations and climatological analysis

Francesco Manconi[1,2], Alessandro Battaglia[1], Matthew L. Walker McLinden[3], Bernat Puigdomenech Treserras[4], and Pavlos Kollias[4,5]

[1]Department of Mechanical and Aerospace Engineering (DIMEAS), Politecnico di Torino, Turin, Italy
[2]Department of Environment, Land and Infrastructure Engineering (DIATI), Politecnico di Torino, Turin, Italy
[3]NASA Goddard Space Flight Center, Greenbelt, MD, USA
[4]Department of Atmospheric and Oceanic Sciences, McGill University, Montreal, QC, Canada
[5]School of Marine and Atmospheric Sciences, Stony Brook University, Stony Brook, NY, USA

**Correspondence:** francesco.manconi@polito.it

**Abstract.** The Doppler spectral width retrieved from the EarthCARE Cloud Profiling Radar (CPR) could provide valuable information on cloud dynamics, turbulence, and hydrometeor variability. Its interpretation is challenging, however, because the measured signal is dominated by spacecraft-motion-induced Doppler broadening and is further affected by pulse-pair estimation uncertainty and instrumental effects. Preliminary analysis of the operational Level-1B products also reveals a systematic negative bias relative to the broadening expected under nominal observation geometry.

Pulse-pair simulations based on synthetic in-phase and quadrature (I/Q) signals show that finite-sample statistics, thermal noise, and receiver saturation may explain the intrinsic retrieval uncertainty but not the observed negative bias. Together with the apparent inconsistency between the lag-0 and lag-1 autocovariance quantities in the Level-1B products, the former representing received echo power, these results motivate an empirical recalibration of the lag-1 autocovariance using the theoretically expected Doppler broadening in homogeneous stratiform ice clouds as a reference.

Across a global one-year dataset, the recalibrated spectral width exhibits distinct statistical signatures as a function of temperature, reflectivity, and along-track reflectivity gradient, which is used to assess non-uniform beam-filling effects. Although spacecraft-motion broadening and pulse-pair estimation uncertainty remain the dominant contributors, the recalibrated product retains some geophysical variability. Spectral-width broadening over high-power surface clutter is also consistent with receiver-saturation effects. Overall, the results indicate that, for the DA baseline release, the EarthCARE Level-1B spectral-width product is unsuitable for quantitative applications even after recalibration, but can provide useful qualitative and diagnostic information.

## 1 Introduction

The EarthCARE (Earth Cloud Aerosol and Radiation Explorer) mission is a joint mission of the European Space Agency (ESA) and the Japan Aerospace Exploration Agency (JAXA) designed to improve the understanding of cloud, aerosol, precipitation and radiation processes and their role in the Earth's climate system. The mission payload combines active and passive remote

https://doi.org/10.5194/egusphere-2026-6816
Preprint. Discussion started: 17 November 2026
© Author(s) 2026. CC BY 4.0 License.

sensing instruments, including the Cloud Profiling Radar (CPR), the Atmospheric Lidar (ATLID), the Multi-Spectral Imager (MSI) and the Broad-Band Radiometer (BBR), enabling synergistic observations of atmospheric structure and radiative transfer processes (Illingworth et al., 2015).

The EarthCARE CPR is the first spaceborne cloud radar operating at W-band (94 GHz), with Doppler capabilities (Puigdomènech Treserras et al., 2025; Imura et al., 2026). While Doppler velocities have been validated (Kim et al., 2025) and exploited for global observations of cloud vertical motions and microphysical variability (Galfione et al., 2025; Kim et al., 2026), the Doppler spectral width ($\sigma_D$) has received comparatively less attention. This quantity is related to turbulence, vertical wind shear and hydrometeor variability within the radar sampling volume (Doviak and Zrnić, 1993), making it a potentially valuable observable for the study of cloud dynamics and precipitation processes.

Interpreting $\sigma_D$ measurements from space is fundamentally challenging. Because of the spacecraft's high orbital velocity ($\sim$7.6 km s$^{-1}$) and the finite radar footprint ($\sim$750 m), the measured spectral width is largely dominated by motion-induced Doppler broadening. The framework of Sy and Tanelli (2023) expresses the measured spectral variance as $\sigma_D^2 = \sigma_I^2 + \sigma_{sat}^2$, where $\sigma_I$ is the intrinsic atmospheric spectral width associated with variability in line-of-sight air motion and hydrometeor terminal velocity, and $\sigma_{sat}$ is the broadening induced primarily by spacecraft motion and the finite antenna beamwidth. Under nominal EarthCARE geometry, $\sigma_{sat}$ alone is expected to be about 3.73 m s$^{-1}$ for homogeneous beam filling; non-uniform beam filling (NUBF) may either broaden or narrow the observed spectrum. Because $\sigma_I$ in smooth stratiform ice clouds is typically below $\sim$1 m s$^{-1}$, atmospheric dynamics contribute only a small fraction of the measured spectral variance. Broader spectra also decorrelate more rapidly, further complicating estimation of $\sigma_I$.

Preliminary analyses of the EarthCARE Level-1B Doppler products reveal cloud-target spectral widths systematically lower than those predicted from motion-induced Doppler fading for the CPR observation geometry. This discrepancy suggests an inconsistency in the relative amplitude calibration of the lag-0 and lag-1 autocovariances of the received voltage signals. We therefore propose a physically based calibration method that uses the theoretically predicted motion-induced Doppler broadening in regions with low intrinsic spectral width, such as homogeneous stratiform ice clouds, to refine this cross-calibration. The recalibration enables a physically consistent climatology across cloud regimes. We further assess estimator uncertainty and potential receiver-saturation bias using simulations of the I/Q voltage signals. Finally, we examine the extent to which the atmospheric contribution to spectral width can be separated from the dominant spacecraft-motion broadening.

This study uses EarthCARE CPR Level-1B C-NOM products from processing baseline DA.

## 2 Pulse-Pair Estimation of Spectral Width

The Doppler spectral width is estimated operationally through pulse-pair (PP) processing of the complex radar signal based on the temporal autocorrelation properties of the received signal (Doviak and Zrnić, 1993; Bringi and Chandrasekar, 2001). The received voltages may be represented as a sequence of complex in-phase and quadrature samples:

$$V_n = I_n + iQ_n, \tag{1}$$

https://doi.org/10.5194/egusphere-2026-6816
Preprint. Discussion started: 17 November 2026
© Author(s) 2026. CC BY 4.0 License.

where $I_n$ and $Q_n$ are the in-phase and quadrature components of the received signal for pulse index $n$, with the pulses separated by the pulse repetition interval (PRI). The Doppler information is encoded in the temporal phase evolution of the complex voltages.

All pulse-pair estimators are based on the sample autocovariance functions:

$$\hat{R}_m = \frac{1}{M-m} \sum_{n=1}^{M-m} V_n V_{n+m}^*, \tag{2}$$

where $m$ denotes the lag, $M$ is the number of pulses and $(\cdot)^*$ denotes complex conjugation. In particular:

- $\hat{R}_0$, the lag-0 autocovariance estimate, corresponds to the total received power;
- $\hat{R}_1$, the lag-1 autocovariance estimate, is related to the temporal correlation of the signal.

Under the assumption of a Gaussian Doppler spectrum (see Appendix A), the lag-1 autocovariance magnitude is directly related to the Doppler spectral width through:

$$\hat{\sigma}_D = \frac{v_{Nyq}}{\pi} \sqrt{2 \ln \left( \frac{\hat{R}_0 - N_f}{|\hat{R}_1|} \right)}, \tag{3}$$

where $v_{Nyq}$ is the Nyquist velocity and $N_f$ is the spatially and temporally uncorrelated thermal-noise contribution (noise floor). The pulse-pair estimator assumes a Gaussian Doppler spectrum and stationarity over the integration interval (Doviak and Zrnić, 1993; Bringi and Chandrasekar, 2001). Violations of these assumptions may introduce substantial estimation errors. Moreover, as the argument of the logarithm involves finite-sample estimates, in some cases it may happen that $(\hat{R}_0 - N)/|\hat{R}_1| < 1$, yielding $\sigma_D$ values that have no physical meaning and therefore need to be excluded from any analysis.

The physical interpretation of the estimator is straightforward. A narrow Doppler spectrum corresponds to slowly decorrelating complex signals and therefore large values of $|R_1|$ at fixed signal power, whereas broad Doppler spectra produce rapid decorrelation and smaller lag-1 autocovariance magnitudes.

Estimators of $\sigma_D$ are therefore based on estimates of the noise-subtracted power and of $R_1$. The performance of the estimator is governed by the signal-to-noise ratio (SNR), the number of independent samples and the normalized spectral width (Doviak and Zrnić, 1993). Broad spectral widths are particularly challenging for estimating $R_1$. This is the case for spaceborne Doppler radars, where spacecraft motion induces substantial Doppler broadening due to the Doppler fading effect, amounting to approximately 3.73 m s$^{-1}$ under nominal EarthCARE geometry (Sy and Tanelli, 2023).

However, preliminary analyses of the EarthCARE Level-1B (C-NOM) products revealed measured spectral widths around 2.5 m s$^{-1}$, narrower than predicted by theory (see Appendix B), as shown in Fig. 1. To determine whether pulse-pair estimation biases, for example those associated with broad spectra, can explain the observed narrowing, we developed a simulation framework based on synthetic I/Q signals. The simulator reproduces the EarthCARE processing chain (Appendix A) and radar specifications (Table 1). Appendix A1 discusses the adopted noise-floor value.

https://doi.org/10.5194/egusphere-2026-6816
Preprint. Discussion started: 17 November 2026
© Author(s) 2026. CC BY 4.0 License.

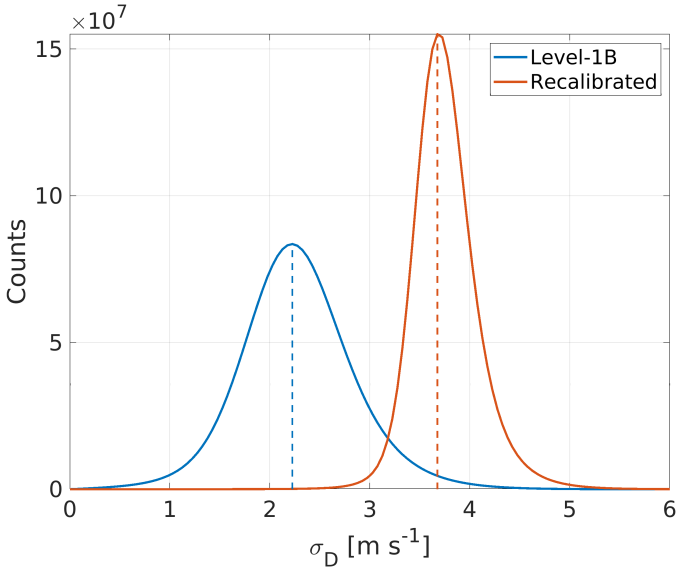



**Figure 1.** Distribution of $\sigma_D$ values, selected within smooth stratiform ice regions. The two curves show the distribution as reported in the Level-1B products (blue), and renormalized to $\sigma_{sat} = 3.73$ m s$^{-1}$ as described in Sect. 3 (red). Dashed lines represent median values.

**Table 1.** Radar specifications adopted for simulation of EarthCARE complex voltage time series.

| Property | Symbol | Value | Units |
|---|---|---|---|
| Radar frequency | $f_0$ | 94 | GHz |
| Pulse Repetition Frequency | $PRF$ | 7.1 | kHz |
| Integration number | $N_{IQ}$ | 418 | - |
| Reflectivity noise floor | $N_f$ | -23.75 | dBZ |
| Along-track Antenna beamwidth | $\theta_{3dB}^{AT}$ | 0.092 | deg |
| Cross-track Antenna beamwidth | $\theta_{3dB}^{CT}$ | 0.09 | deg |

### 2.1 Performance of Spectral Width Estimator

The statistical behaviour of the pulse-pair spectral-width estimator depends on the Doppler spectral width and signal-to-noise ratio (SNR). Reflectivity estimation depends primarily on signal power, whereas mean Doppler velocity depends on the phase of the lag-1 autocovariance. In contrast, the spectral-width estimator depends on the logarithm of the ratio of the lag-0 and lag-1 autocovariance magnitudes.

The error associated with the pulse-pair spectral width estimator is characterized by a Monte Carlo simulation where constant vertical profiles of Gaussian Doppler spectra with different SNR levels and spectral widths are used to generate time series of

https://doi.org/10.5194/egusphere-2026-6816
Preprint. Discussion started: 17 November 2026
© Author(s) 2026. CC BY 4.0 License.

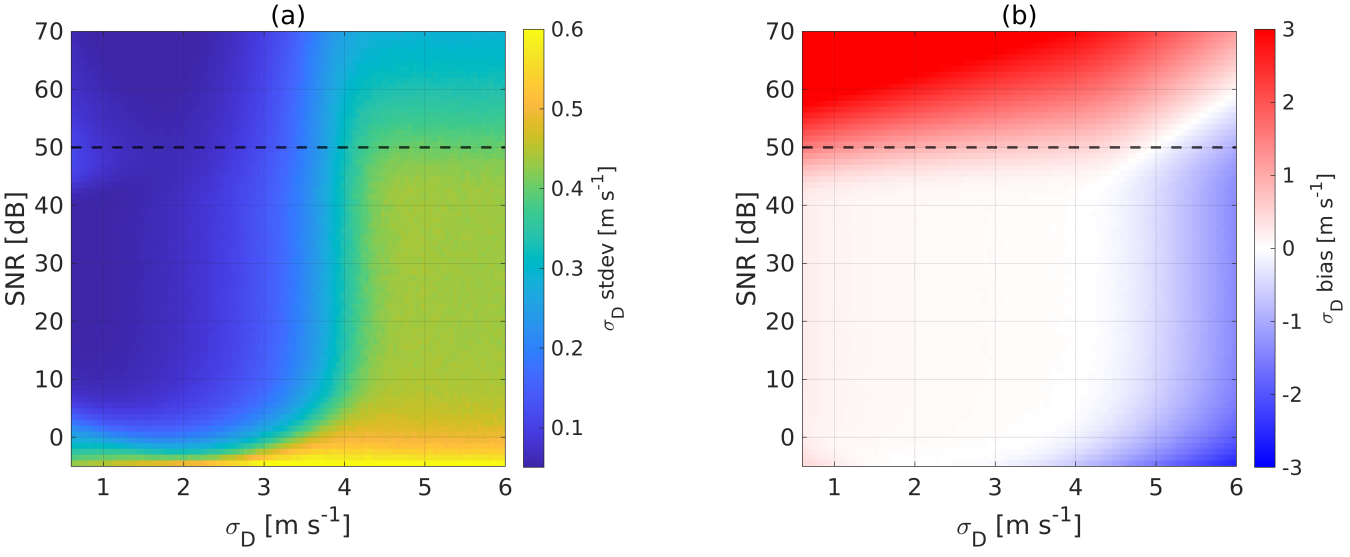



**Figure 2.** Pulse-pair estimator error for spectral width, using EarthCARE CPR specifications and acquisition scheme. Panel (a): standard deviation; panel (b): bias. Black dashed lines represent saturation thresholds (see Sect. 2.2).

I/Q (sampled at 100 m in range). For each combination of SNR and prescribed spectral width values, roughly $8 \cdot 10^6$ realisations are used to compute the bias and standard deviation of the spectral width estimator. The simulation includes the effect of receiver saturation as well. In fact, the $\sigma_D$ estimator combines quantities derived from two different signal-processing chains: the received echo power, derived from the logarithmic detector measurements, and $R_1$, appearing in the denominator inside the $\sigma_D$ pulse-pair estimator formula (Eq. 3), derived from the linear receiver that tends to saturate at high SNRs (EarthCARE/CPR Project Team, 2023).

Saturation is introduced only in the $\hat{R}_1$ estimates through clipping of the in-phase and quadrature voltages (Battaglia and Kollias, 2014) of the form:

$$I_{clip} = \max[-V_{max}, \min(I, V_{max})],$$
$$Q_{clip} = \max[-V_{max}, \min(Q, V_{max})], \tag{4}$$

where $V_{max}$ denotes the saturation threshold, selected such that saturation occurs for signal powers greater 50 dB SNR.

Figure 2 shows the estimator standard deviation (a) and bias (b) as functions of prescribed $\sigma_D$ and SNR.

The black dashed line marks the saturation threshold above which nonlinear clipping of the complex voltages is applied (Sect. 2.2). We first discuss the nominal estimator behaviour, i.e. for SNR values below this threshold.

As shown in Fig. 2, the pulse-pair estimator is affected primarily by finite-sample statistics, thermal noise, and signal decorrelation. At low SNR, thermal noise progressively dominates the lag-1 autocovariance, increasing the estimation variance. This effect becomes more pronounced for broad Doppler spectra, where the intrinsic reduction of lag-1 autocovariance makes the

https://doi.org/10.5194/egusphere-2026-6816
Preprint. Discussion started: 17 November 2026
© Author(s) 2026. CC BY 4.0 License.

estimator increasingly sensitive to statistical fluctuations. Similarly, the estimator is typically unbiased at low spectral widths but has an increasingly higher negative bias when moving towards large spectral widths (panel (b)).

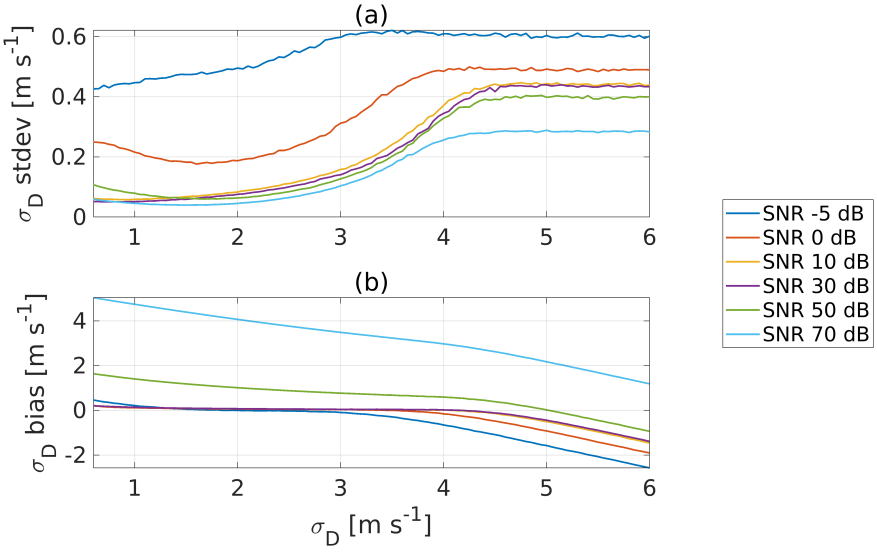



**Figure 3.** Spectral width pulse-pair estimator error characterization using EarthCARE CPR specifications, 1D slices of Fig. 2 taken at different constant SNR. Panel (a): standard deviation; panel (b): bias.

The region above the dashed black line in Fig. 2 corresponds to the onset of simulated nonlinear clipping, implemented by saturating the in-phase and quadrature components at approximately 50 dB SNR (Sect. 2.2).

Fig. 3 illustrates the error trends more quantitatively. For sufficiently high SNR, without saturation effects, panel (b) shows that the estimator is essentially unbiased over the range 2–4 m s$^{-1}$, while panel (a) indicates a standard deviation of approximately 0.2–0.3 m s$^{-1}$. As the prescribed spectral width increases beyond ∼4–5 m s$^{-1}$, the estimator becomes progressively noisier, reaching a plateau of about 0.42 m s$^{-1}$, while also developing an increasing negative bias. Conversely, narrower spectra are retrieved with both lower variance and smaller bias.

Overall, the simulations show that pulse-pair estimation effects alone cannot explain the systematic ∼1 m s$^{-1}$ narrowing observed in the EarthCARE products. While they may account for a significant fraction of the noisiness of the estimates, the persistent underestimation of the spectral widths points to additional instrumental or processing effects, motivating the empirical recalibration introduced in Sect. 3.

## 2.2 Signal Saturation and Clipping

Conversely, the Level-1B product exhibits systematically high spectral widths in regions of highly reflective ground clutter. We attribute this behaviour to saturation in the CPR linear receiver.

The simple clipping model described in Eq. 4 explains two distinct features that are clearly visible above the saturation threshold in Fig. 2. In the standard deviation map, after crossing the saturation threshold, the noisiness of the estimates goes

https://doi.org/10.5194/egusphere-2026-6816
Preprint. Discussion started: 17 November 2026
© Author(s) 2026. CC BY 4.0 License.

down significantly for broad spectra, while it remains essentially unchanged under roughly 4 m s$^{-1}$ of intrinsic $\sigma_D$. At the same time, in panel (b), overestimation becomes significant with increasing SNR across all spectra, but particularly for narrow ones. This effect on the bias characterization can be explained easily by looking at the formula for the $\sigma_D$ estimator (Eq. 3). The lag-0 numerator term, derived from the logarithmic receiver, is unaffected by clipping and continues to increase with signal power, whereas the denominator term is clipped. The spectral width therefore keeps increasing with the SNR once the saturation threshold is surpassed.

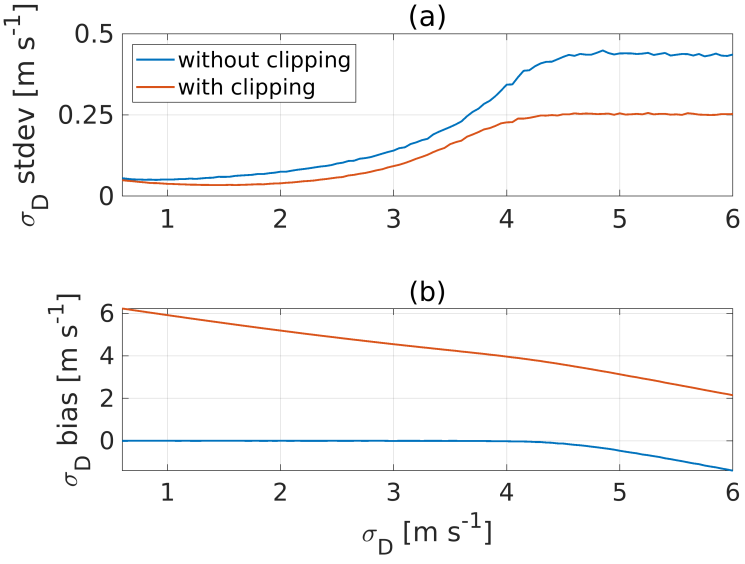



**Figure 4.** Comparison between non-saturated and saturated error statistics at SNR = 60 dB.Panel (a): standard deviation; panel (b): bias. The blue curve is computed without clipping, while the red curve has been computed clipping the $|\hat{R}_1|$ term in Eq. 3.

Fig. 4 compares the estimation error statistics with and without nonlinear clipping at an SNR of 60 dB. Clipping (red) reduces the estimator variance (a) but introduces a large positive bias (b).

## 3 Spectral Width Recalibration

A systematic discrepancy emerges when the EarthCARE Level-1B spectral-width product is compared with the theoretical broadening expected under nominal observation geometry. Figure 5 shows a representative, mainly stratiform scene with some convective cells. Even within extensive homogeneous ice clouds, retrieved $\sigma_D$ is systematically below the value expected from motion-induced broadening and exhibits substantial noise.

The pulse-pair simulations presented in Sect. 2.1 show that finite-sample statistics, thermal noise and receiver nonlinearities cannot explain the systematic narrowing of approximately 1 m s$^{-1}$ observed in the Level-1B ver. DA product. Together with the absence of documented physical units for the Level-1B lag-1 autocovariance (Japan Aerospace Exploration Agency (JAXA),

https://doi.org/10.5194/egusphere-2026-6816
Preprint. Discussion started: 17 November 2026
© Author(s) 2026. CC BY 4.0 License.

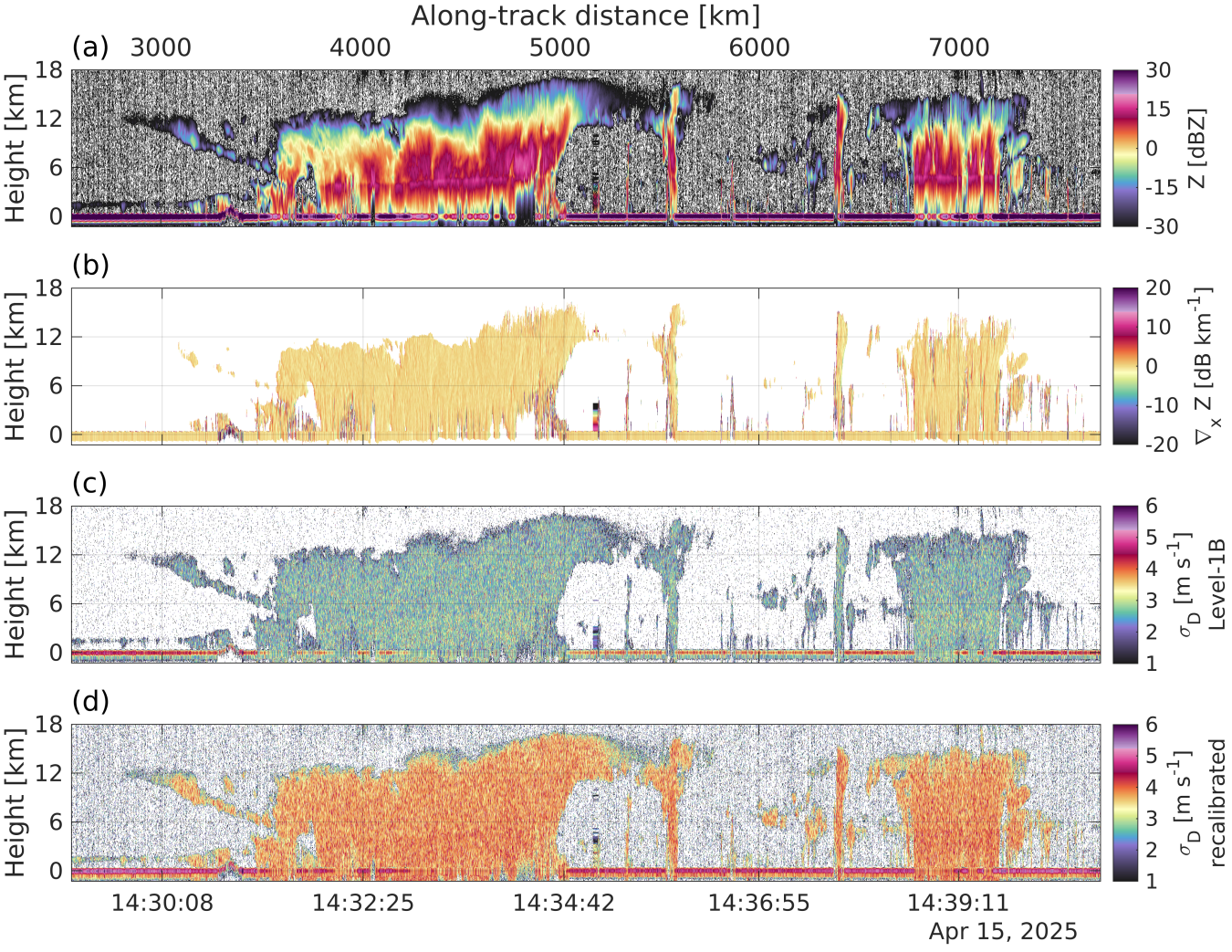



**Figure 5.** Representative stratiform scene extracted from two consecutive Level-1B granules, “05004H" and “05005A", DA baseline. Panel(a): noise-subtracted reflectivity. Panel (b): along-track reflectivity gradient. Paanel (c): original Level-1B spectral width. Pnale (d):recalibrated spectral width. Each quantity is plotted as a function of height vs time/along-track distance (bottom/top x-axis labels).

2025; EarthCARE/CPR Project Team, 2023), this finding suggests an inconsistency in the processing or relative calibration of this quantity, although its origin remains uncertain.

An empirical multiplicative factor $K$ is therefore introduced, applied to the lag-1 autocovariance. Following Sy and Tanelli (2023), smooth stratiform ice clouds are adopted as a reference regime, since they are expected to exhibit weak turbulence, lim-
145 ited vertical wind shear and approximately homogeneous beam-filling conditions. Under these assumptions, the observed spectral width should asymptotically approach the deterministic broadening induced by spacecraft motion (see details in App. B),

https://doi.org/10.5194/egusphere-2026-6816
Preprint. Discussion started: 17 November 2026
© Author(s) 2026. CC BY 4.0 License.



which is approximately equal to:

$$\sigma_{sat} = v_{\perp} \frac{\theta_{3dB}}{4\sqrt{\ln 2}} \approx 3.73 \text{ m s}^{-1} = \sigma_{calibr}, \tag{5}$$

where $\theta_{3dB}$ is the along-track antenna beamwidth in radians, 0.092 deg for EarthCARE's CPR (Japan Aerospace Exploration Agency (JAXA), 2025), and $v_{\perp}$ is the component of the spacecraft Earth-centred Earth-fixed (ECEF) velocity perpendicular to the boresight, computed to be approximately 7.74 km s$^{-1}$ on average around one orbit from Level-1B data. For simplicity, the antenna is assumed to have a circular beam with $\theta_{3dB} = \theta_{3dB}^{AT}$. A detailed discussion about the formula in Eq. 5 and the definition of the $v_{\perp}$ value is provided in Appendix B.

The multiplicative factor $K$ is computed by imposing the theoretical broadening value as calibration target and inverting the pulse-pair estimation formula:

$$\frac{v_{Nyq}}{\pi} \sqrt{2 \ln \left( \frac{\hat{R}_0 - N_f}{K |\hat{R}_1|} \right)} = \sigma_{calibr} = 3.73 \text{ m s}^{-1}. \tag{6}$$

The calibration points are selected using the ESA Level-2A products interpolated onto the Level-1B grid, specifically the C-TC and C-FMR products, version BD (Tatarevic et al., 2025, 2026). Using the simplified convective classification mask, points with $T < 0°$C, flagged as stratiform, and with SNR between 10 and 40 dB are selected. The calibration factor $K$ is determined as the median of the values computed for all selected points within each granule. Each granule covers approximately one-eighth of an orbit, allowing the calibration to account for potential geographical and temporal variability. At least $10^3$ valid points are required; otherwise, $K$ is assigned the median value derived from the full one-year climatological ensemble.

The estimator formula can then be applied using the recalibrated $\hat{R}_1$ to compute the recalibrated spectral width, as shown in panel (d) of Fig. 5 for the case study. The red curve in Fig. 1 shows the effect of the recalibration on the spectral width distribution in smooth stratiform ice regions, with a shift toward the reference value and a decrease in dispersion.

By setting the calibration target $\sigma_{calibr} = \sigma_D$ equal to $\sigma_{sat}$, zero intrinsic atmospheric spectral width $\sigma_I$ is assumed, as explained in Appendix B. Therefore, this calibration introduces a small negative bias. A conservative estimate of this error can be obtained by assuming $\sigma_I = 1$ m s$^{-1}$, twice a commonly quoted value of 0.5 m s$^{-1}$ (Hagihara et al., 2023) for stratiform ice clouds. The actual spectral width would then be $\sqrt{\sigma_{sat}^2 + \sigma_I^2} = \sqrt{3.73^2 + 1^2} \simeq 3.86$ m s$^{-1}$, corresponding to a bias of approximately $-0.13$ m s$^{-1}$, or $-3.4\%$.

### 3.1 Aircraft Observations

Recent validation activities based on high-resolution observations from the 2025 NASA Goddard Lidar Observation and Validation Experiment (GLOVE) field campaign provide independent evidence supporting the interpretation in Sect. 3. The NASA Cloud Radar System (CRS) airborne W-band radar (Walker McLinden et al., 2021) flew on the NASA ER-2 aircraft in a series of coordinated underflights of the EarthCARE satellite.

The high-resolution airborne-radar data (115 m vertical resolution sampled every 14 m; 185–224 m horizontal resolution sampled every 50 m) included reflectivity, Doppler velocity, and Doppler spectral width. These three products were used to

https://doi.org/10.5194/egusphere-2026-6816
Preprint. Discussion started: 17 November 2026
© Author(s) 2026. CC BY 4.0 License.

simulate the EarthCARE Doppler velocity spectrum and spectral width using the reported EarthCARE altitude and Earth Centered Earth Fixed (ECEF) velocity from the EarthCARE Level 1B data file. As discussed in Appendix B, for targets stationary with respect to the Earth-fixed frame, the radial and perpendicular velocity associated with spacecraft motion can be computed directly from the spacecraft ECEF velocity. The simulations assumed a Gaussian along-track antenna pattern with a half-power one-way beamwidth of 0.092°.

To simulate the EarthCARE CPR Doppler spectrum, each high-resolution CRS pixel within the EarthCARE beam is represented by a Gaussian spectrum. Its width is set by the CRS-derived spectral width, and its centre velocity combines the CRS vertical Doppler velocity with the radial velocity associated with the EarthCARE ECEF velocity and along-track pointing angle. The spectra are summed across the footprint and subsequently averaged using the CPR along-track averaging and vertical weighting functions. The resulting spectrum yields the idealized CPR Doppler velocity and spectral width.

Although GLOVE provided useful observations from four EarthCARE underpasses, we selected the 20 February 2025 flight for quantitative comparison. This underpass was over a winter storm with some orographic features. The data included large sections of relatively homogeneous reflectivity and mean Doppler velocity, with very low Doppler velocity spectral widths measured by CRS. CRS and CPR data from the EarthCARE_CPR_L1B_CPR_NOM product Ver. DA (Japan Aerospace Exploration Agency (JAXA), 2024) granule “04169D" are shown in Figure 6.

Figure 6 shows excellent agreement in reflectivity between CRS and CPR. The area of quantitative comparison (within 30 km of the overpass and 4 km to 6 km height above sea level) corresponds to a match in time of within 150 seconds due to the approximate 200 m $s^{-1}$ velocity of the NASA ER-2 aircraft. The reflectivities match with a mean difference of 0.6 dB and a standard deviation of 0.8 dB.

The spectral-width fields do not agree well. The CRS-derived spectral width indicates very weak turbulence, with a mean below 0.2 m $s^{-1}$. The modeled CPR spectral width in the region of interest after accounting for the antenna pattern and satellite motion is 3.71 m $s^{-1}$ with a standard deviation of 0.07 m $s^{-1}$, which is consistent with the low underlying spectral width combined with the relatively homogeneous reflectivity environment. The mean CPR L1B Ver. DA spectral width in the area of comparison is 2.60 m $s^{-1}$ with a standard deviation of 0.48 m $s^{-1}$.

We recalculated the CPR Doppler spectral width using the standard algorithm in the CPR algorithm theoretical basis document (ATBD) (EarthCARE/CPR Project Team, 2023), after adjusting the calibration of the covariance-coefficient magnitude from the Level-1B file to match the simulation and theoretical predictions. This adjusted spectral width has a mean of 3.71 m $s^{-1}$ and a standard deviation of 0.34 m $s^{-1}$.

Histograms of the spectral widths are shown in Fig. 7. As predicted, the CPR Doppler velocity spectral width better matches predictions after adjusting the covariance coefficient magnitude. There is a residual positive skewness to the CPR retrieved spectral width, which is also visible as hot pixels in Fig. 6 (f). This skewness may be caused by a difference in the receiver matched filtering between the power and covariance coefficient receivers, but is outside the scope of this analysis.

https://doi.org/10.5194/egusphere-2026-6816
Preprint. Discussion started: 17 November 2026
© Author(s) 2026. CC BY 4.0 License.

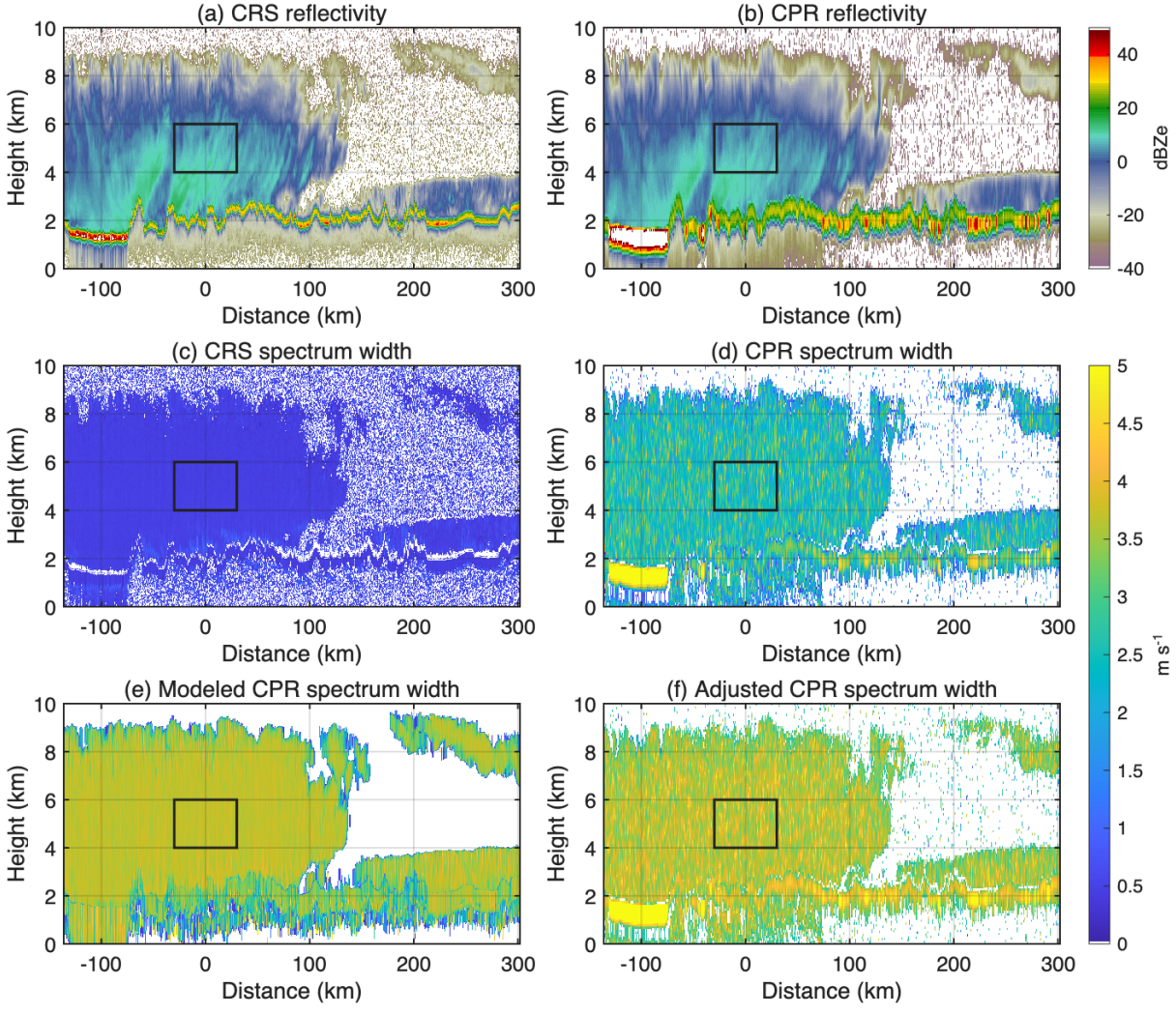



**Figure 6.** Data from the February 20, 2025 GLOVE flight. (a) CRS reflectivity. (b) CPR reflectivity. (c) CRS-derived spectral width (d) CPR L1B spectral width (e) Modeled CPR spectral width using CRS reflectivity, Doppler, and spectral width. (f) Adjusted CPR spectral width using a recalibrated covariance coefficient magnitude. On all plots, the area used for quantitative comparisons is shown as a black box.

## 4 Climatology of Recalibrated Spectral Width

Following recalibration, we examine the retrieved spectral width across atmospheric and surface regimes to assess whether systematic geophysical signatures remain observable.

We compute spectral-width density plots as functions of reflectivity, temperature, and along-track reflectivity gradient. Reflectivity is primarily used as a proxy for signal strength, hydrometeor content and scattering regime. Temperature provides a physically meaningful reference variable, allowing liquid- and ice-phase cloud populations to be distinguished while account-

https://doi.org/10.5194/egusphere-2026-6816
Preprint. Discussion started: 17 November 2026
© Author(s) 2026. CC BY 4.0 License.

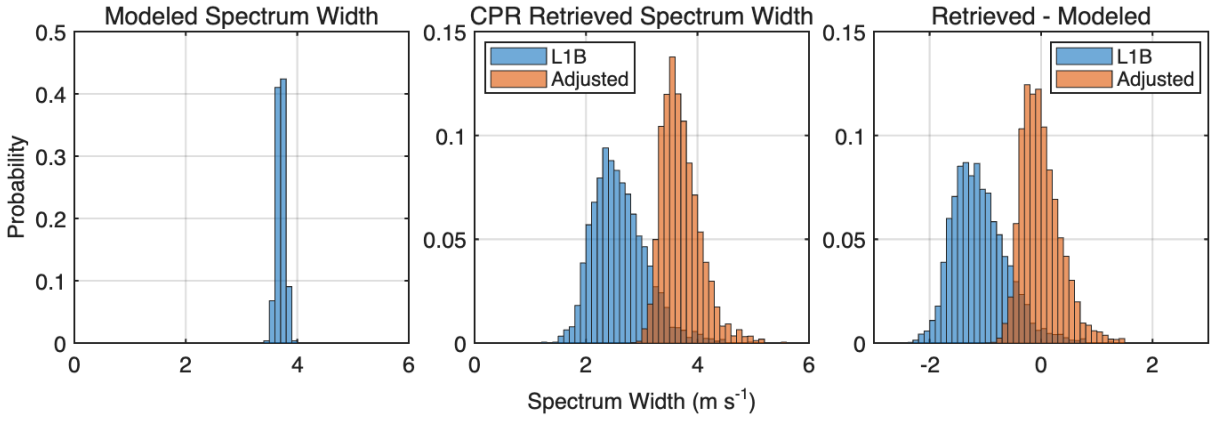



**Figure 7.** Histograms of Doppler spectral width in the region of interest highlighted in Fig. 6. (Left) The modeled CPR spectral width has a mean of 3.71 m $s^{-1}$ and a standard deviation of 0.07 m $s^{-1}$. (Centre) The Level-1B Ver. DA spectral width has a mean of 2.60 m $s^{-1}$ and a standard deviation of 0.48 m $s^{-1}$. After adjustment of the covariance-coefficient magnitude, the CPR spectral width has a mean of 3.71 m $s^{-1}$ and a standard deviation of 0.34 m $s^{-1}$. (Right) The adjusted retrieval agrees more closely with the modeled spectral width and has a lower standard deviation.

ing for the dependence of cloud microphysics on altitude, independently of latitude and season. The along-track reflectivity gradient is used as a proxy for non-uniform beam filling (NUBF), which is expected to play a major role in Doppler spectral broadening and narrowing (Sy and Tanelli, 2023).

The following regimes are considered:

- stratiform clouds, where intrinsic broadening is dominated by ice microphysics (Kollias et al., 2014);
- multiple scattering-contaminated regions, where wide spectral broadening is caused by high turbulence associated with deep convection (Kollias et al., 2018, 2022a) and by the multiple scattering mechanism itself (Battaglia and Tanelli, 2011);
- surface clutter return, separated over land and water, which present cases of extreme broadening near the clutter power peak and potentially indicate saturation effects. An effort is made to relate the behaviour in these regimes to the nonlinear clipping of the complex voltages discussed in Sect. 2.2.

The different regimes are identified based on the ESA Level-2A CPR Target Classification (C-TC) and the Feature Mask and Reflectivity (C-FMR) products (Kollias et al., 2022b), interpolated onto the Level-1B grid. One year of observations (2025) is considered.

### 4.1 Atmospheric Targets

Figures 8 and 9 summarize the climatological behaviour of the recalibrated spectral width for the analyzed atmospheric regimes. To reduce the impact of noise-induced artefacts, only observations with SNR larger than 10 dB are considered.

https://doi.org/10.5194/egusphere-2026-6816
Preprint. Discussion started: 17 November 2026
© Author(s) 2026. CC BY 4.0 License.

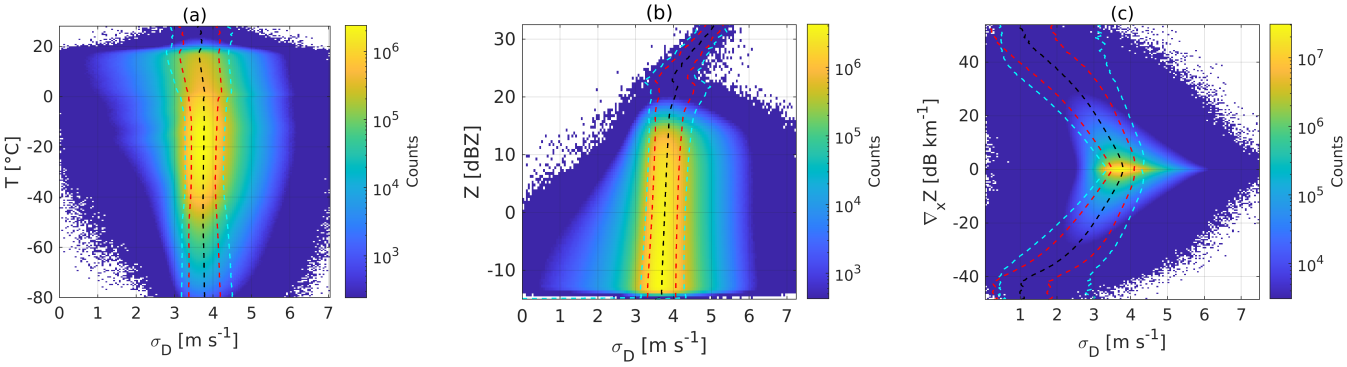



**Figure 8.** Climatology of recalibrated spectral width in stratiform clouds. The distributions are shown as a function of atmospheric temperature (a), radar reflectivity (b) and along-track reflectivity gradient (c). The black dashed line denotes the mean spectral width within each vertical bin, while the red dashed lines indicate $\pm 1$ standard deviation.

Stratiform clouds exhibit relatively compact spectral-width distributions centred around the reference value of 3.73 m s$^{-1}$, consistent with weak turbulence, limited vertical shear and approximately homogeneous beam-filling conditions. Panel (a) shows a clear transition across the melting: the ice phase displays narrower distributions, with standard deviations of about 0.3 m s$^{-1}$, whereas the liquid phase becomes noticeably broader, approaching 0.5 m s$^{-1}$.

As shown in Fig. 3, at high SNR the expected pulse-pair estimator noise is about 0.3 m s$^{-1}$; it is therefore the dominant source of variability in stratiform-ice retrievals. The increase to a standard deviation to 0.5 m s$^{-1}$ is consistent with greater variability among liquid-hydrometeor populations. Deviations from the simulated estimator noise may thus reflect geophysical characteristics of the sampled regime.

Panel (b) also shows a weak increase of $\sigma_D$ with reflectivity, suggesting a modest contribution from a broader particle size distribution. Panel (c), however, shows the clearest feature: the dependence on the along-track reflectivity gradient. Increasing along-track reflectivity gradient magnitudes are associated with progressively narrower spectral widths and larger dispersion. This behaviour appears consistently across both the analyzed atmospheric regimes and suggests that NUBF predominantly tends to narrow Doppler spectra.

In Fig. 9, multiple-scattering regions exhibit systematically broader and noisier spectral width distributions, as expected from the combined effects of multiple scattering itself, stronger atmospheric variability and departures from the Gaussian spectrum assumption underlying the pulse-pair estimator. Panel (a) shows a considerably stronger temperature dependence than in stratiform clouds, with spectral width increasing steadily towards colder ice-phase conditions, where large ice particles and deep convective structures favour multiple scattering. This trend is also consistent with the typical vertical structure of these systems: the coldest observations generally correspond to cloud-top regions, where reflectivities can still reach 15–20 dBZ, whereas reflectivity progressively decreases towards warmer temperatures at lower altitudes. As discussed in Sect. 2.1, high received powers are associated with a slight overestimation of the retrieved spectral width, which may therefore contribute

https://doi.org/10.5194/egusphere-2026-6816
Preprint. Discussion started: 17 November 2026
© Author(s) 2026. CC BY 4.0 License.

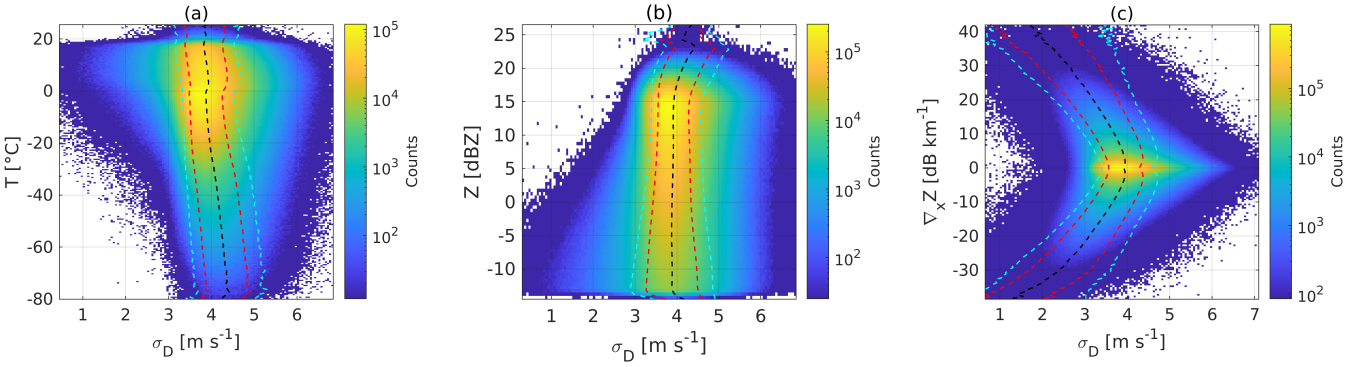



**Figure 9.** Climatology of recalibrated spectral width in multiple-scattering regions. The distributions are shown as a function of atmospheric temperature (a), radar reflectivity (b) and along-track reflectivity gradient (c). Black and red dashed lines respectively represent the mean and $\pm 1$ standard deviation inside each vertical bin, cyan dashed lines the 10th and 90th percentiles.

to the observed temperature dependence. In the liquid phase, high-mass-content regions exhibit increased dispersion, likely associated with stronger hydrometeor variability and precipitation processes.

Unlike the stratiform regime, panel (b) shows a weaker and more dispersed dependence on reflectivity, likely reflecting the combined effects of attenuation, convection and strong NUBF. Panel (c) also shows the characteristic narrowing associated with increasing along-track reflectivity gradients, indicating that this behaviour is not restricted to weakly turbulent clouds but persists also in highly scattering environments.

Overall, the climatological analysis reveals systematic differences between atmospheric regimes, indicating that the recalibrated spectral width retains some physically meaningful variability. However, the dominant contribution from spacecraft-motion broadening, together with pulse-pair estimation uncertainty and saturation effects, still strongly limits the direct interpretation of the retrieved values.

### 4.2 Surface Return

Surface clutter observations represent a useful test case for investigating the behaviour of the pulse-pair estimator near the limits of the receiver dynamic range at high SNR conditions.

As shown in the case study in Fig. 5, very high $\sigma_D$ values occur near the surface-return peak. This pattern is ubiquitous except in regions where strong cloud attenuation significantly reduces the clutter signal. Since the intrinsic Doppler variability of the surface clutter itself is expected to remain relatively small, such broadening is unlikely to originate from genuine geophysical Doppler dispersion alone and instead strongly suggests the presence of instrumental nonlinearities.

Figure 11 shows the relationship between $\sigma_D$ and reflectivity in clutter regimes. As in Fig. 2(b), saturation becomes apparent at about 20–25 dBZ, corresponding approximately to an SNR of 45 dB. Consistent with the error characterization, clipping effects are visible about 5 dB below the simulated 50 dB threshold. As $|R_1|$ becomes progressively bounded, $\sigma_D$ approaches a dependence proportional to $[\ln(\hat{R}_0) - C_{R_1}]^{1/2}$, where $C_{R_1}$ is nearly constant.

https://doi.org/10.5194/egusphere-2026-6816
Preprint. Discussion started: 17 November 2026
© Author(s) 2026. CC BY 4.0 License.

The distribution over land is more irregular than over the ocean. Land surfaces are known to exhibit a much broader range of normalized radar cross section (NRCS) values than water surfaces because radar backscatter depends strongly on vegetation, soil moisture, surface roughness and terrain characteristics (Long and Ulaby, 2015; Manconi et al., 2025). This pattern is also evident in the climatological ensemble: Fig. 10 shows that the NRCS distribution over land is more irregular than that over water. Both distributions are asymmetric and exhibit secondary peaks, which also produces some unevenness in the water distributions in Fig. 11, although less than over land.

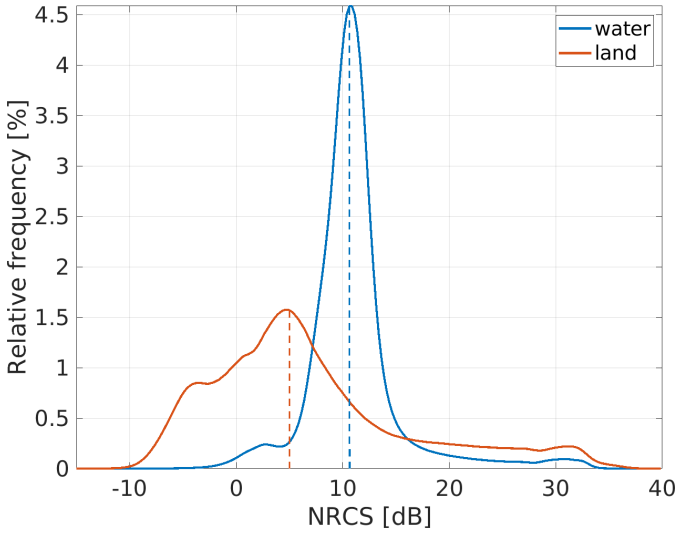



**Figure 10.** Distributions of NRCS, in clear sky conditions and corrected for gaseous attenuation, over water (blue) and land (red) surface targets. Dashed lines represent median values.

In general, the behaviour is remarkably consistent with the clipping simulations presented in Sect. 2.2 and strongly suggests that nonlinear receiver effects constitute a major contribution to the observed spectral width variability in high-power regimes.

The simulated curve (magenta) agrees broadly with the observed trends, supporting the interpretation that instrumental nonlinearities, rather than intrinsic Doppler variability, account for a substantial fraction of the large spectral widths in strong-return regimes. However, the simulations overestimate broadening near saturation onset and underestimate it for very high surface returns (above 35 dBZ). These discrepancies may reflect the simplified saturation model; the true receiver response is likely more complex.

## 5 Conclusions

This work investigated the Doppler spectral width retrieved from the EarthCARE Cloud Profiling Radar (CPR) through theoretical analysis, pulse-pair simulations based on synthetic I/Q signals and a one-year climatological characterization of the Level-1B observations, from the DA baseline. The objective was to assess whether the spectral-width product is physically

https://doi.org/10.5194/egusphere-2026-6816
Preprint. Discussion started: 17 November 2026
© Author(s) 2026. CC BY 4.0 License.

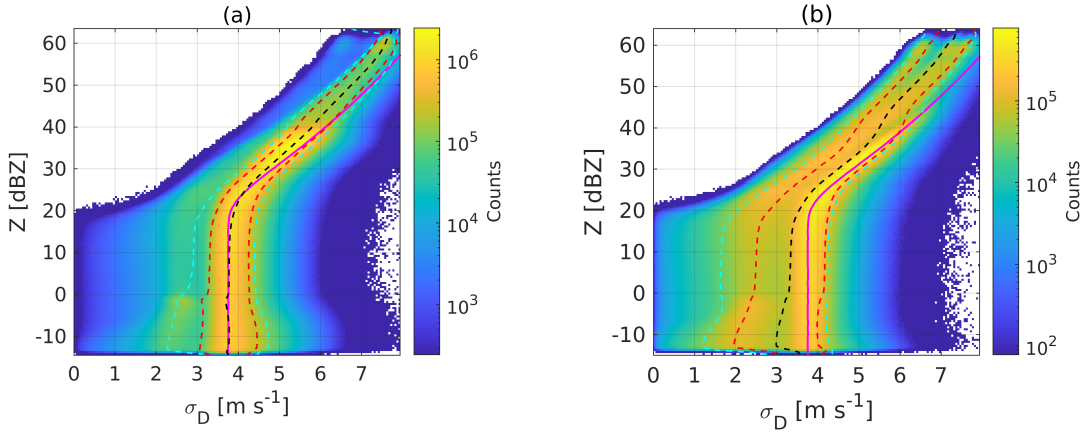



**Figure 11.** Statistics of recalibrated $\sigma_D$ versus reflectivity in ground clutter regimes: (a) over water, (b) over land. Black and red dashed lines respectively represent the mean and $\pm 1$ standard deviation inside each vertical bin, cyan dashed lines the 10th and 90th percentiles. Magenta curves show the values predicted by the simulations at 3.73 m s$^{-1}$ prescribed $\sigma_D$.

consistent with the expected EarthCARE observation geometry and to quantify the contribution of instrumental and processing effects to the retrieved signal.

Theoretical considerations indicate that, under nominal EarthCARE geometry, the measured spectral width is expected to be dominated by spacecraft-motion-induced broadening, leading to values of approximately 3.7–4 m s$^{-1}$ under homogeneous beam-filling conditions. In contrast, the Level-1B product systematically exhibits narrower spectral widths, particularly in smooth stratiform ice clouds. Inspection of the Level-1B autocovariance quantities further suggests that the lag-1 covariance is not calibrated consistently with the lag-0 power estimate, motivating the introduction of an empirical recalibration of the quantity, estimated using smooth stratiform ice regimes as a reference.

The pulse-pair simulations show that finite-sample statistics, thermal noise and receiver nonlinearities all contribute to uncertainties in the spectral-width estimates. In the broadening-dominated regime expected for EarthCARE, the intrinsic estimator uncertainty stays at approximately 0.2–0.3 m s$^{-1}$ under good SNR conditions, increasing for broader spectra and lower signal-to-noise ratios. Although these effects account for part of the retrieval uncertainty, they are insufficient to explain the systematic narrowing observed in the operational product, supporting the need for a lag-1 covariance calibration.

After applying the described recalibration and recomputing the spectral width, the climatological analysis reveals consistent features between atmospheric regimes. Multiple-scattering regions exhibit broader spectral width distributions than stratiform ice, while systematic variations are also observed as a function of reflectivity and along-track reflectivity gradient. These results indicate that, after recalibration, the product still retains some meaningful geophysical information on the different atmospheric conditions, but the motion-induced broadening and pulse-pair estimator error remain the main drivers of the spectral width signal.

Overall, the analysis supports two conclusions:

https://doi.org/10.5194/egusphere-2026-6816
Preprint. Discussion started: 17 November 2026
© Author(s) 2026. CC BY 4.0 License.

1. as of the DA baseline, the EarthCARE Level-1B spectral width product should not be interpreted quantitatively without additional calibration of the lag-1 covariance;

2. even after recalibration the retrieval appears to carry some geophysical features, though the Doppler fading introduced by the satellite motion and the large pulse-pair estimation error still dominate the signal.

Therefore, the spectral-width variable is currently more suitable for qualitative and diagnostic applications than for quantitative retrieval of geophysical information.

Future work should identify the origin of the lag-1 covariance scaling and incorporate an operational spectral-width calibration. Because this study uses the Level-1B resolution (∼500 m along track), further integration may also reduce pulse-pair estimation noise and improve the information recoverable from the signal.

## Appendix A: Simulation of Complex I and Q Time Series

We simulated synthetic in-phase and quadrature (I/Q) radar signals using the autocovariance-based methodology of Battaglia et al. (2025). The framework generates oversampled stochastic complex radar time series from prescribed vertical profiles of Doppler moments while preserving the temporal autocovariance required for pulse-pair processing. $N_{IQ}$ denotes the number of active pulses averaged within the ∼500 m along-track integration window of the EarthCARE Level-1B products.

Unlike classical inverse fast Fourier transform (IFFT) techniques commonly adopted for stationary Doppler simulations, the autocovariance-based approach directly constructs the temporal correlation matrix associated with the radar signal. This formulation is particularly suitable for spaceborne Doppler radars because it naturally accommodates nonstationary conditions, arbitrary pulse separations and decorrelation induced by spacecraft motion, multiple scattering and antenna scanning.

For a prescribed Doppler spectrum $S(v)$, the corresponding temporal autocorrelation function is obtained through the Fourier transform:

$$R(\tau) = \int_{-\infty}^{+\infty} S(v) \exp\left(-i\frac{4\pi}{\lambda} v\tau\right) dv, \tag{A1}$$

where $R(\tau)$ is the complex autocorrelation at lag $\tau$, $S(v)$ is the Doppler power spectrum and $\lambda$ is the radar wavelength.

If the Doppler spectrum is assumed Gaussian:

$$S(v) = \frac{P}{\sqrt{2\pi}\sigma_D} \exp\left[-\frac{(v - v_D)^2}{2\sigma_D^2}\right], \tag{A2}$$

where $P$ is the signal power, $v_D$ is the mean Doppler velocity, $\sigma_D$ is the Doppler spectral width, the temporal autocorrelation becomes:

$$\rho(\tau) = P \exp\left(-\frac{8\pi^2\sigma_D^2\tau^2}{\lambda^2}\right) \exp\left(-i\frac{4\pi v_D \tau}{\lambda}\right), \tag{A3}$$

which explicitly shows that increasing spectral width produces faster temporal decorrelation of the complex signal. From Eq. A3, the expression for the $\sigma_D$ pulse-pair estimator (Eq. 3) is obtained.

https://doi.org/10.5194/egusphere-2026-6816
Preprint. Discussion started: 17 November 2026
© Author(s) 2026. CC BY 4.0 License.

For a sequence of $M$ pulses, the $M \times M$ autocovariance matrix of the complex signals can be constructed from Eq. (A1) as:

$$\mathbf{R}_{ij} = \rho(\tau_i - \tau_j), \tag{A4}$$

where $\tau_i$ and $\tau_j$ denote the acquisition times of pulses $i$ and $j$. Thus correlations up to lag $M-1$ are accounted for.

$\mathbf{R}$ is Hermitian and positive definite and can therefore be factorized through Cholesky decomposition:

$$\mathbf{R} = \mathbf{L}\mathbf{L}^{\dagger}, \tag{A5}$$

where $(\cdot)^{\dagger}$ denotes the Hermitian transpose.

A vector of independent circular complex Gaussian random variables:

$$\mathbf{y}_S = [y_1, y_2, \ldots, y_M]^T \tag{A6}$$

with $y_k = \frac{1}{\sqrt{2}}(\xi_k + i\eta_k)$ and $\xi_k, \eta_k \sim \mathcal{N}(0,1)$ (normally distributed random numbers with zero mean and unit standard deviation) is then transformed into correlated complex voltages according to:

$$\mathbf{V}_S = \mathbf{L}\mathbf{y}_S. \tag{A7}$$

The resulting vector:

$$\mathbf{V}_S = [V_1, V_2, \ldots, V_k, \ldots, V_M]^T = [I_1 + iQ_1, I_2 + iQ_2, \ldots, I_k + iQ_k, \ldots, I_M + iQ_M]^T \tag{A8}$$

contains synthetic I/Q samples with the prescribed autocovariance properties and Doppler spectrum.

As the noise is spatially and temporally decorrelated, it is generated separately from the noise-free signal, as:

$$\mathbf{V}_N = \mathbf{y}_N \sqrt{N_f}, \tag{A9}$$

where $N_f$ is the thermal noise floor corresponding to the profile and $\mathbf{y}_N$ is a separate realization of independent circular complex Gaussian random variables.

The radar acquisition includes both nominal "RF on" observations and dedicated "RF off" silent-state measurements used for noise characterization (Japan Aerospace Exploration Agency (JAXA), 2025; EarthCARE/CPR Project Team, 2023).

To reproduce this scheme, the synthetic I/Q simulations are segmented into blocks of $M = 22$ consecutive pulses (Sy and Tanelli, 2023), followed by a silent interval of duration $2 \cdot PRI$. The autocovariance matrix is constructed for each block and $M$ complex I/Q samples are generated for each block independently. Stationarity is assumed as the displacement on the surface due to the satellite motion is negligible with respect to the radar footprint itself. A sequence of $N_{IQ}$ I/Qs is generated by concatenating the 22 samples of each single block. Complete decorrelation is assumed between consecutive blocks, which is reasonable because the EarthCARE lag-2 autocorrelation is typically below 0.015. The operation is repeated for each height bin.

https://doi.org/10.5194/egusphere-2026-6816
Preprint. Discussion started: 17 November 2026
© Author(s) 2026. CC BY 4.0 License.

To introduce range correlation due to the radar receiver response and the pulse shape, the signal and noise oversampled vertical profiles are then convolved, independently of each other. The range weighting functions for the noise $h_N$ and for the active signal $h_S$ are defined as follows, respectively:

$$h_N(r-r_0) = \begin{cases} C_N \left[\alpha + \frac{1-\alpha}{2}\cos\left(2\pi\frac{|r-r_0|}{L/2}\right)\right], & |r-r_0| \le \frac{L}{4} \\ 0, & |r-r_0| > \frac{L}{4} \end{cases} \tag{A10}$$

$$h_S(r-r_0) = \begin{cases} C_S \left[\left(1-\frac{|r-r_0|}{L/2}\right)\left(\alpha + \frac{1-\alpha}{2\pi}\sin\left(2\pi\frac{|r-r_0|}{L/2}\right)\right)\right], & |r-r_0| \le \frac{L}{2} \\ 0, & |r-r_0| > \frac{L}{2} \end{cases} \tag{A11}$$

where $\alpha = 0.54$, $r$ is the position along the vertical profile, $r_0$ is the center position of the radar range gate, $L$ is the pulse width and $C_S$ and $C_N$ are normalization constants. Note that this convolution is much simpler than the procedure described in Schutgens (2008), nonetheless it creates the right range correlation of the complex voltages.

The total complex voltages are obtained simply as the sum of the two contributions:

$$\tilde{\mathbf{V}} = \tilde{\mathbf{V}}_S + \tilde{\mathbf{V}}_N, \tag{A12}$$

where the tilde indicates the convolved voltages. Pulse-pair autocovariance estimates are then computed only within each block of active transmission:

$$R_m^b = \frac{1}{M-m}\sum_{k=1}^{M-m} \tilde{V}_k \tilde{V}_{k+m}^*, \tag{A13}$$

where $m$ is the autocovariance lag. The autocovariances within the blocks are then averaged together across $N_B$ blocks to reproduce the effective integration $N_{IQ}$ number corresponding to the ∼500 m along-track integration length of the EarthCARE Level-1B products:

$$\hat{R}_m = \frac{1}{N_b}\sum_{b=1}^{N_b} R_m^b. \tag{A14}$$

From $\hat{R}_0$ and $\hat{R}_1$ the power, mean Doppler velocity and Doppler spectral width can be estimated with classic pulse-pair processing (Doviak and Zrnić, 1993).

This framework is suitable not only for the EarthCARE Doppler signal but also for future spaceborne Doppler radars (e.g. PMM (Iki et al., 2025), FALCON (Voosen, 2026), WIVERN (Illingworth et al., 2018; Battaglia, Alessandro and Manconi, Francesco and Recupero, Massimiliano and Cambiotti, Cinzia and Coppola, Marco and Parodi, Antonio and Tridon, Frederic and Mantovani, Simone and Kollias, Pavlos and Nolan, David S. and Kleinherenbrink, Marcel and Pourshamsi, Maryam, 2026)).

https://doi.org/10.5194/egusphere-2026-6816
Preprint. Discussion started: 17 November 2026
© Author(s) 2026. CC BY 4.0 License.

### A1 Noise floor value

A climatological analysis was carried out to compute an average value of the noise floor $N_f$ in reflectivity for the I/Q simulations.

From the Level-1B Product Description Document (Japan Aerospace Exploration Agency (JAXA), 2025), $N_f$ is provided in the `noiseFloorPower` variable in power units for each along-track ray. Conversion from received power $P_r$ to reflectivity $Z$ is described in the Algorithm Theoretical Basis Document (EarthCARE/CPR Project Team, 2023), as follows:

$$Z = 10^{18} \frac{\lambda^4}{\pi^5 |K_w|^2} C_r \frac{P_r}{P_t} r^2, \tag{A15}$$

where $|K_w|^2 = 0.75$, $r$ is the range, $P_t$ is the transmitted power and the coefficient $C_r$ is directly provided in the Level-1B data as the `radarCoefficient` variable. At each ray, range is computed for every height bin and the conversion formula is applied to the noise floor quantity.

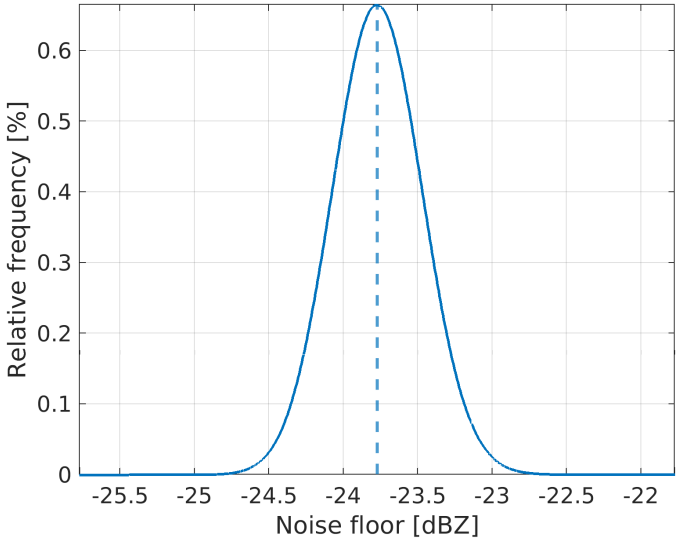



**Figure A1.** Distribution of the CPR noise floor expressed in reflectivity units for 2025. Dashed line: median value.

Figure A1 shows the noise floor distribution in dBZ units for every available ray and corresponding range gate across 2025. The mean value is around $-23.75$ dBZ and it represents a global average considering any effects due to seasonality, location, altitude or atmospheric variability. The standard deviation is about 0.3 dB.

Figure A2 shows maps of the global climatology of the noise floor in logarithmic power and reflectivity units over the 2025 year, with $1^\circ \times 1^\circ$ resolution. For conversion from power to reflectivity units, a reference range was chosen. In particular, it was set to the range to the intercept with the WGS84 ellipsoid, i.e. the range corresponding to the zero geodetic height. At each ray, this quantity is usually larger than the mean of the range gates, so the climatological maps show higher mean values than what Fig. A1 shows, which is the trade-off chosen to study the global variability of this quantity. In general, in panels (a) and (c),

https://doi.org/10.5194/egusphere-2026-6816
Preprint. Discussion started: 17 November 2026
© Author(s) 2026. CC BY 4.0 License.

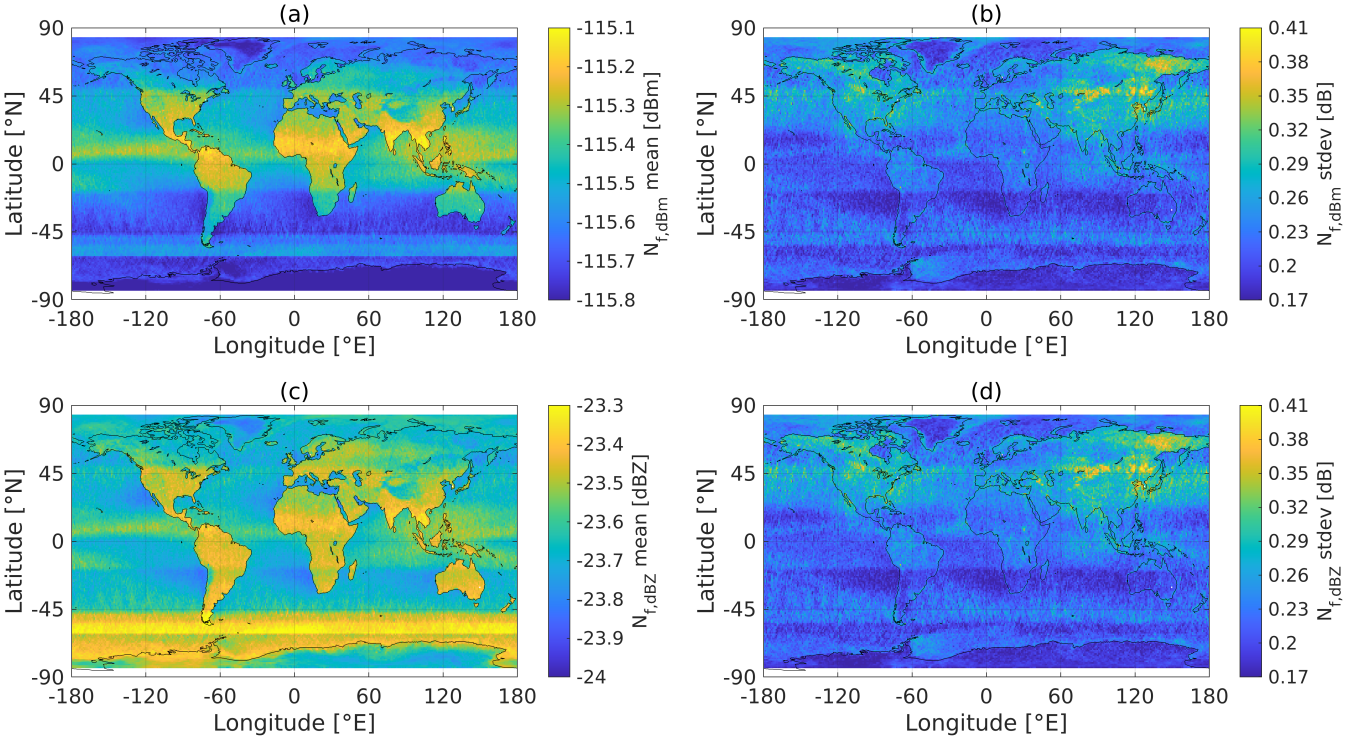



**Figure A2.** Global maps of noise floor climatology for 2025, at a $1^\circ \times 1^\circ$ resolution. Panel (a): mean values of $N_f$ in log power units (dBm). Panel (b): standard deviation values computed from $N_f$ in dBm. Panel (c): mean values of $N_f$ in log reflectivity units (dBZ). Panel (d): standard deviation values computed from $N_f$ in dBZ.

the noise floor shows a trend with latitude, and appears higher over land than over water, which can be respectively attributed to the variation of brightness temperature and to the differences in emissivity between the two surface types. An anomalous pattern can be seen south of $45^\circ$ S, a bright band of high values: the feature is very apparent, but its cause was not investigated as it was considered out of the scope for this study. Even taking into account the aforementioned anomaly, the overall dynamic range across the globe is less than 1 dB. Standard deviation values in panels (b) and (d) are consistent between the two units and present maximum values of $\sim$0.45 dB, so the value shows limited variability at both local and global scales.

The mean value of $-23.75$ dBZ in Fig. A1 has been set as the constant noise floor for the I/Q simulations in Section A, which is a figure that better represents a typical global value at an average height. Although the noise-floor climatology contains some irregularities, this brief analysis is intended only to characterize its variability and justify the value adopted in Table 1; an in-depth climatological analysis is beyond the scope of this study.

https://doi.org/10.5194/egusphere-2026-6816
Preprint. Discussion started: 17 November 2026
© Author(s) 2026. CC BY 4.0 License.

## Appendix B: Motion-Induced Spectral Width Broadening Calculation

The Doppler spectral broadening induced by spacecraft motion originates from the variation of the line-of-sight (LOS) velocity across the finite antenna footprint. Even in the absence of atmospheric motions, different portions of the illuminated volume experience different radial velocities because the radar-target relative velocity is projected onto slightly different viewing directions. Generally, this mechanism is commonly referred to as velocity shearing (Doviak and Zrnić, 1993, Sect. 5.3) or Doppler fading (Sy and Tanelli, 2023).

In terms of radar moments, instrument motion induces artificial variability in Doppler shift across the footprint. This contribution is represented by the satellite-motion broadening term $\sigma_{sat}$.

In this section we derive a simplified analytical expression for $\sigma_{sat}$ from the radar-equation expression for spectral variance (Doviak and Zrnić, 1993). Then, the obtained expression is numerically evaualated for the EarthCARE orbit and compared with a discrete integration of the radar equation, in order to assesses the variability in $\sigma_{sat}$ along the satellite trajectory.

### B1 Mathematical Derivation

Assuming uniform beam filling and uniform target velocities across the backscattering volume, the Doppler spectrum is entirely determined by the distribution of relative LOS velocities within the illuminated volume. The corresponding spectral variance is therefore the second central moment of the power-weighted LOS:

$$\sigma_{sat}^2 = \frac{\int_V G^2(\theta,\phi)\,(v_{LOS} - \bar{v}_{LOS})^2\,dV}{\int_V G^2(\theta,\phi)\,dV}, \tag{B1}$$

where $G$ is the antenna gain pattern and

$$\bar{v}_{LOS} = \frac{\int_V G^2 v_{LOS}\,dV}{\int_V G^2\,dV} \tag{B2}$$

is the power-weighted mean Doppler velocity.

The LOS velocity at each illuminated point is obtained from the relative radar-target velocity projected onto the local viewing direction,

$$v_{LOS} = (\mathbf{v}_T - \mathbf{v}_{SC}) \cdot \hat{\mathbf{r}}, \tag{B3}$$

where $\mathbf{v}_{SC}$ and $\mathbf{v}_T$ are the spacecraft and target velocities, respectively, measured in some inertial reference frame, and $\hat{\mathbf{r}}$ is the unit vector directed from the radar to the target.

https://doi.org/10.5194/egusphere-2026-6816
Preprint. Discussion started: 17 November 2026
© Author(s) 2026. CC BY 4.0 License.

Choosing an Earth-centred inertial frame to express vector quantities, the velocity of a target stationary with respect to the rotating Earth is

$$\mathbf{v}_T = \boldsymbol{\omega}_E \times \mathbf{r}_T, \tag{B4}$$

where $\boldsymbol{\omega}_E$ is the Earth's angular velocity vector. Similarly, the spacecraft velocity can be decomposed as

$$\mathbf{v}_{SC} = \mathbf{v}_{SC,E} + \boldsymbol{\omega}_E \times \mathbf{r}_{SC}, \tag{B5}$$

where $\mathbf{v}_{SC,E}$ denotes the spacecraft velocity relative to the rotating Earth-Fixed, Earth-Centred (ECEF) reference, expressed in the same inertial basis as the other quantities. Introducing the radar-target relative position vector

$$\mathbf{r} = \mathbf{r}_T - \mathbf{r}_{SC} = r\,\hat{\mathbf{r}}, \tag{B6}$$

and by substituting these expressions in Eq. (B3), the relative velocity term can therefore be written as

$$\mathbf{v}_T - \mathbf{v}_{SC} = -\mathbf{v}_{SC,E} + \boldsymbol{\omega}_E \times \mathbf{r}. \tag{B7}$$

The term $\boldsymbol{\omega}_E \times \boldsymbol{\rho}$ on the right-hand side has no component along the radar-target LOS, as it is always perpendicular to $\hat{\mathbf{r}}$, and therefore does not contribute to any Doppler shift. Consequently, for any target stationary in the ECEF reference frame, the LOS velocity can be expressed exactly as

$$v_{LOS} = -\mathbf{v}_{SC,E} \cdot \hat{\mathbf{r}}. \tag{B8}$$

Thus, although the inertial velocity associated with the Earth's rotation varies across the illuminated volume, this variation does not independently contribute to the LOS velocity. The spatial variation of $v_{LOS}$ across the beam is instead determined by the projection of the spacecraft ECEF velocity onto the different viewing directions.

For a symmetric Gaussian antenna and sufficiently small beamwidth, the LOS velocity varies approximately linearly across the footprint. Only the component of the radar-target relative velocity perpendicular to the beam centre contributes to this variation, while the component parallel to the beam merely shifts the mean Doppler velocity without changing its variance. Decomposing $\mathbf{v}_{SC,E}$ into components parallel and perpendicular to the boresight direction $\hat{\mathbf{u}}_{bs}$, the magnitude of the transverse component is

$$v_\perp = \left\| \left( \mathbf{I} - \hat{\mathbf{u}}_{bs} \hat{\mathbf{u}}_{bs}^T \right) \mathbf{v}_{SC,E} \right\| = \sqrt{\left\| \mathbf{v}_{SC,E} \right\|^2 - \left( \mathbf{v}_{SC,E} \cdot \hat{\mathbf{u}}_{bs} \right)^2}. \tag{B9}$$

To develop the integral expression, a beam-centred reference frame is introduced, with the $z$-axis along the boresight and the $x$-axis along the transverse component of $-\mathbf{v}_{SC,E}$. For small angular deviations from boresight, the unit LOS vector is approximated as

$$\hat{\mathbf{r}} \simeq \begin{bmatrix} \theta \cos\phi \\ \theta \sin\phi \\ 1 \end{bmatrix}, \tag{B10}$$

https://doi.org/10.5194/egusphere-2026-6816
Preprint. Discussion started: 17 November 2026
© Author(s) 2026. CC BY 4.0 License.

where $\theta$ and $\phi$ are the polar and azimuthal angles, respectively. Using Eq. (B8), the LOS velocity then becomes

$$v_{LOS} = -\mathbf{v}_{SC,E} \cdot \hat{\mathbf{r}} \simeq v_{\parallel} + v_{\perp}\theta\cos\phi, \tag{B11}$$

where $v_{\parallel}$ denotes the boresight LOS velocity. The parallel component therefore determines the mean Doppler shift, whereas the transverse component determines, to first order, the variation of LOS velocity across the beam. Thus, as $\bar{v}_{LOS} = v_{\parallel}$ exclusively induces a Doppler shift, the variance is determined only by $(v_{LOS} - \bar{v}_{LOS})^2 = (v_{\perp}\theta\cos\phi)^2$. Factoring out the range dependence and assuming small-angle approximation, Eq. (B1) becomes

$$\sigma_{sat}^2 = \frac{\int_0^{\pi}\int_0^{2\pi} G^2(\theta)\,(v_{\perp}\theta\cos\phi)^2\,\theta\,d\phi\,d\theta}{\int_0^{\pi}\int_0^{2\pi} G^2(\theta)\theta\,d\phi\,d\theta}. \tag{B12}$$

For a circular Gaussian antenna pattern, $G(\theta) = \exp\left[-4\ln 2\left(\frac{\theta}{\theta_{3dB}}\right)^2\right]$, with angles expressed in radians, the integral can be evaluated under the narrow-beam approximation $\theta_{3dB} \ll \pi$. COnsidering the identities

$$\frac{\int_0^{\infty}\theta^3 e^{-\theta^2}d\theta}{\int_0^{\infty}\theta e^{-\theta^2}d\theta} = 1, \qquad \int_0^{2\pi}\cos^2\phi\,d\phi = \pi, \tag{B13}$$

we obtain

$$\sigma_{sat} = v_{\perp}\frac{\theta_{3dB}}{4\sqrt{\ln 2}}, \tag{B14}$$

which represents the motion-induced Doppler broadening under uniform beam-filling conditions.

### B2 Numerical Simulation

In this section, full orbital simulation are performed, with the objective of characterizing the latitude dependence of $v_{\perp}$ and consequently of $\sigma_{sat}$.

A Keplerian orbit is assumed, such that all orbital elements, except true and mean anomaly, remain constant. Given an arbitrary starting epoch and set of orbital parameters (see Table B1), the mean anomaly is propagated in time assuming a constant mean motion, then the satellite Earth-centred position and velocity in the Earth-Centred Inertial (ECI) frame are computed (Vallado and McClain, 2013, Chap. 2). The WGS84 ellipsoid properties are used to compute the local geodetic nadir direction, which is the CPR antenna pointing reference direction (Kollias et al., 2022b). Earth's oblateness induces a variation in the nadir pointing direction which is a function of the satellite latitude and altitude (Markley and Crassidis, 2014, Sect. 2.6.3).

The values in Table B1 have been chosen as a proxy among all 2025 data to give the most conservative estimates of $v_{\perp}$, corresponding to a minimum of $a$, a maximum of $e$ and a minimum of $i$. The RAAN $\Omega$ does not contribute to any variability

https://doi.org/10.5194/egusphere-2026-6816
Preprint. Discussion started: 17 November 2026
© Author(s) 2026. CC BY 4.0 License.

**Table B1.** Orbital parameters adopted for the simulations of the EarthCARE orbit.

| Property | Symbol | Value | Units |
|---|---|---|---|
| Semi-major axis | $a$ | 6770.4 | km |
| Eccentricity | $e$ | 0.001313 | - |
| Inclination | $i$ | 96.992 | deg |
| Right Ascension of the Ascending Node | $\Omega$ | 0 | deg |
| Argument of Perigee | $\omega$ | 0 | deg |
| Initial True Anomaly | $\nu$ | 0 | deg |

of $v_\perp$ as it simply rotates the orbital plane around Earth's axis, so an arbitrary value is set. In the circular orbit case, $\omega$ and $\nu$ only shift the satellite starting point but not the amplitude, but for non-zero eccentricity an additional variation in the satellite velocity along the orbit is introduced, and the latitude dependence of $v_\perp$ changes. Therefore, for the non-zero eccentricity cases, a full sweep of all possible $\omega$ and $\nu$ combinations is performed to get the lower and upper bounds of the shaded areas in Fig. B1.

As reported in the Level-1B ver. DA products header data, EarthCARE CPR's beam is slightly elliptic, with $\theta_{3dB}^{AT} = 0.092°$ in the along-track direction, while $\theta_{3dB}^{CT} = 0.09°$ in the cross-track direction. For simplicity of calculations, and given the fact that the main contribution to the motion-induced spectral width broadening is essentially directed in the along-track direction, the beam has been assumed to be circular with $\theta_{3dB} = \theta_{3dB}^{AT} = 0.092°$.

Figure B1 shows the $\sigma_{sat}$ and $v_\perp$ values over one EarthCARE orbit. In panel (a), the analytical values of $\sigma_{sat}$ obtained from Eq. B14 are compared with a numerical evaluation of Eq. B1, performed by discretizing the illuminated atmospheric volume and explicitly computing the geometry and radar-target relative ECI velocity of each element. A circular orbit was considered as the baseline for the two curves, in order to isolate the latitude-dependent variability along the orbital trajectory associated with the Earth's rotation and oblateness. The former depends only on the satellite's position relative to the Earth's rotation axis, while, at zero eccentricity, the variation in altitude above the reference ellipsoid is determined solely by latitude. The maximum relative difference between the analytical and numerical results is below 0.01%, and can be attributed mainly to the finite spatial discretization and the approximations adopted in the mathematical derivation of Eq. B14.

Panel (b) shows the corresponding $v_\perp$ values for the simulated orbit. The shaded region represents the range of possible values associated with orbital velocity variations due to orbital eccentricity at a given latitude, accounting for the changing position of perigee and apogee as the line of apsides precesses by a few degrees per day due to the gravitational perturbation induced by Earth's oblateness, also called $J_2$ effect (Curtis, 2020, Sect. 4.7). To compute this envelope, we performed a full sweep over all possible $\omega$ values for each orbital angular position $u = \omega + \nu$ from the ascending node (also known as the argument of latitude). The corresponding true anomaly is $\nu = u - \omega$, thereby sampling all possible positions of the line

https://doi.org/10.5194/egusphere-2026-6816
Preprint. Discussion started: 17 November 2026
© Author(s) 2026. CC BY 4.0 License.

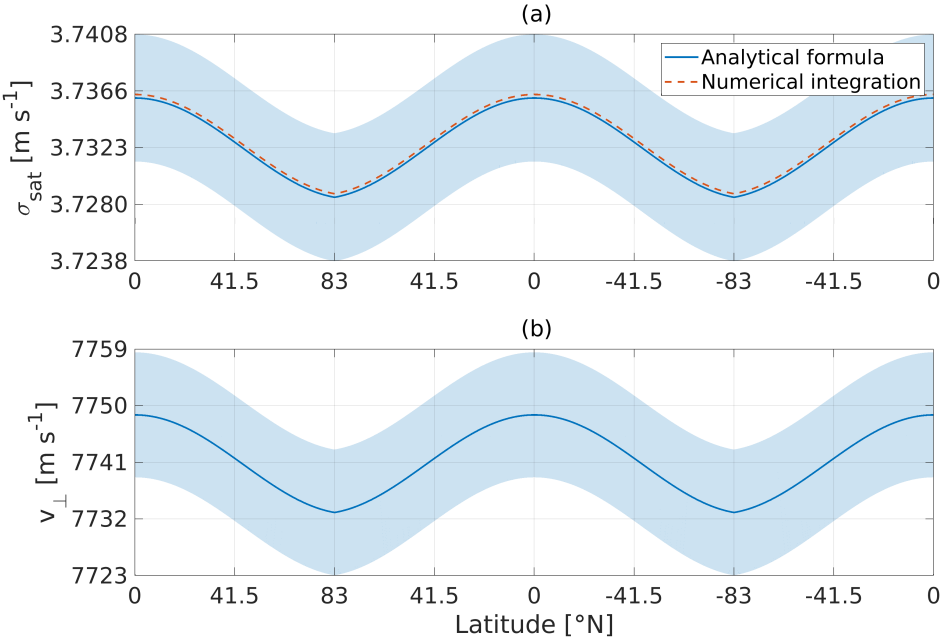



**Figure B1.** Panel (a): motion-induced spectral-width broadening over one simulated EarthCARE circular orbit, when accounting for the latitude-dependent velocity of the atmosphere due to Earth's rotation (with all winds assumed to be identically 0). The analytical values obtained from Eq. B14 (blue line) are compared with the numerical evaluation of Eq. B1 over a discretized atmospheric volume (red dashed line). The shaded region represents the range of velocity deviations at a given latitude that may occur due to the effect of orbit eccentricity and Earth's oblateness, depending on the satellite position between apogee and perigee. Panel (b): corresponding simulated values of $v_\perp$ from which the values in blue in panel (a) have been computed using Eq. B14.

of apsides at that orbital location. As expected, the circular case falls almost perfectly in the middle of the shaded region, approximately representing the mean of the dynamic range at each latitude.

The mean spectral width broadening induced by satellite motion $\sigma_{sat}$ is approximately 3.732 m s$^{-1}$, corresponding to a mean $v_\perp$ of about 7.741 km s$^{-1}$. Accounting for all considered sources of variability, $v_\perp$ has a peak-to-peak variation of approximately 36 m s$^{-1}$, resulting in a dynamic range of about 17.1 mm s$^{-1}$ in $\sigma_{sat}$, equivalent to roughly $\pm 0.23\%$ of the mean value for both quantities.

In conclusion, the ideal broadening values expected for EarthCARE show very limited variability, justifying the use of a constant value of $\sigma_{calibr} = 3.73$ m s$^{-1}$ for the recalibration procedure described in Sect. 3.

*Code and data availability.* The simulation code and derived analysis data are available from the corresponding author upon request. The EarthCARE Cloud Profiling Radar (CPR) Level-1B data used in this study are from the CPR one-sensor received echo power and Doppler product (CPR_NOM, version DA), produced by the Japan Aerospace Exploration Agency (JAXA). These data are available through the

https://doi.org/10.5194/egusphere-2026-6816
Preprint. Discussion started: 17 November 2026
© Author(s) 2026. CC BY 4.0 License.

JAXA G-Portal (https://www.gportal.jaxa.jp) and the European Space Agency (ESA) Multi-Mission Algorithm and Analysis Platform (MAAP; urlhttps://portal.maap.eo.esa.int/), with user registration required (https://doi.org/10.57746/EO.01jdvcydwjf63vpdbjp0vz6v64). The ESA Level-2A CPR Target Classification (C-TC) and Feature Mask and Reflectivity (C-FMR) products, processing baseline BD, are available through ESA MAAP (user registration required; https://doi.org/10.57780/eca-e25465f). Airborne Cloud Radar System (CRS) data from the NASA Goddard Lidar Observation and Validation Experiment (GLOVE) are available at https://har.gsfc.nasa.gov/index.php?section=77. The airborne spectral-width data used in this study were provided separately by NASA GSFC and are available upon request.

*Author contributions.* FM developed the simulation methodology and software, performed the majority of the simulations and data analyses, contributed to the theoretical analysis, and prepared the original manuscript. MLWM independently investigated the satellite-motion-induced spectral broadening and contributed airborne radar data and their analysis, as well as to the theoretical discussion. AB, BPT, and PK conceived the study. AB supervised the research, acquired funding, and contributed to the analysis and manuscript preparation. BPT and PK contributed to the interpretation and discussion of the results. All authors reviewed and edited the manuscript.

*Competing interests.* At least one of the (co-)authors is a member of the editorial board of Atmospheric Measurement Techniques.

*Acknowledgements.* Computational resources were provided by the Mafalda and Felipe high-performance computing (HPC) clusters at Politecnico di Torino. The airborne data were collected as part of the National Aeronautics and Space Administration (NASA) GSFC Lidar Observation and Validation Experiment (GLOVE).

*Financial support.* FM's work was carried out within the Space It Up project, funded by the Italian Space Agency (ASI) and the Ministry of University and Research (MUR) under contract no. 2024-5-E.0 (CUP: I53D24000060005). AB's work was funded by the ESA Scientific Investigations of the Vertical Air MOtion and hydrometeors Sedimentation rates from the EarthCARE CPR (VAMOS) project (AO/1-12468/24/I-AG). The participation of the Cloud Radar System (CRS) in GLOVE, as well as the analysis of CRS data, was funded by the NASA Weather Program.

https://doi.org/10.5194/egusphere-2026-6816
Preprint. Discussion started: 17 November 2026
© Author(s) 2026. CC BY 4.0 License.

## References

Battaglia, A. and Kollias, P.: Impact of Receiver Saturation on Surface Doppler Velocity Measurements From the EarthCARE Cloud Profiling Radar, IEEE Transactions on Geoscience and Remote Sensing, 53, doi 10.1109/TGRS.2014.233589, 2014.

Battaglia, A. and Tanelli, S.: DOMUS: DOppler MUltiple-Scattering Simulator, IEEE Transactions on Geoscience and Remote Sensing, 49, 442–450, https://doi.org/10.1109/TGRS.2010.2052818, 2011.

Battaglia, A., Rizik, A., Sikaneta, I., and Tridon, F.: I and Qs Simulation and Processing Envisaged for Spaceborne Polarization Diversity Doppler Radars, IEEE Transactions on Geoscience and Remote Sensing, 63, 1–14, https://doi.org/10.1109/TGRS.2025.3529672, 2025.

Battaglia, Alessandro and Manconi, Francesco and Recupero, Massimiliano and Cambiotti, Cinzia and Coppola, Marco and Parodi, Antonio and Tridon, Frederic and Mantovani, Simone and Kollias, Pavlos and Nolan, David S. and Kleinherenbrink, Marcel and Pourshamsi, Maryam: Peering Inside Tropical Cyclones With the WIVERN Space-Borne Doppler Radar, Earth and Space Science, 13, https://doi.org/https://doi.org/10.1029/2025EA004680, 2026.

Bringi, V. N. and Chandrasekar, V.: Polarimetric Doppler Weather Radar: Principles and Applications, Cambridge university press, 2001.

Curtis, H. D.: Orbital Mechanics for Engineering Students, Butterworth-Heinemann, 4 edn., ISBN 978-0-12-824025-0, 2020.

Doviak, R. J. and Zrnić, D. S.: Doppler Radar and Weather Observations, Academic Press, https://books.google.nl/books?id=sWljQgAACAAJ, 1993.

EarthCARE/CPR Project Team: EarthCARE Cloud Profiling Radar (CPR) Level 1b Algorithm Theoretical Basis Document (L1b ATBD), Technical Report SEC-140039, Rev. D, Japan Aerospace Exploration Agency (JAXA) and the National Institute of Information and Communications Technology (NICT), 2023.

Galfione, A., Battaglia, A., Puigdomènech Treserras, B., and Kollias, P.: First insights into deep convection by the Doppler velocity measurements of the EarthCARE's Cloud Profiling Radar, EGUsphere, 2025, 1–25, https://doi.org/10.5194/egusphere-2025-1914, 2025.

Hagihara, Y., Ohno, Y., Horie, H., Roh, W., Satoh, M., and Kubota, T.: Global evaluation of Doppler velocity errors of EarthCARE cloud-profiling radar using a global storm-resolving simulation, Atmospheric Measurement Techniques, 16, 3211–3219, https://doi.org/10.5194/amt-16-3211-2023, 2023.

Iki, K., Takayama, S., Nio, T., Okada, K., and Furukawa, K.: Overview of precipitation measuring mission (PMM): the next generation rain mission, in: Remote Sensing of the Atmosphere, Clouds, and Precipitation VIII, edited by Im, E., Yang, S., and Huang, C.-Y., vol. 13262 of *Society of Photo-Optical Instrumentation Engineers (SPIE) Conference Series*, p. 132620C, https://doi.org/10.1117/12.3039878, 2025.

Illingworth, A. J., Barker, H. W., Beljaars, A., Ceccaldi, M., Chepfer, H., Clerbaux, N., Cole, J., Delanoë, J., Domenech, C., Donovan, D. P., Fukuda, S., Hirakata, M., Hogan, R. J., Huenerbein, A., Kollias, P., Kubota, T., Nakajima, T., Nakajima, T. Y., Nishizawa, T., Ohno, Y., Okamoto, H., Oki, R., Sato, K., Satoh, M., Shephard, M. W., Velázquez-Blázquez, A., Wandinger, U., Wehr, T., and van Zadelhoff, G.-J.: The EarthCARE Satellite: The Next Step Forward in Global Measurements of Clouds, Aerosols, Precipitation, and Radiation, Bulletin of the American Meteorological Society, 96, 1311–1332, https://doi.org/10.1175/BAMS-D-12-00227.1, 2015.

Illingworth, A. J., Battaglia, A., Bradford, J., Forsythe, M., Joe, P., Kollias, P., Lean, K., Lori, M., Mahfouf, J.-F., Melo, S., Midthassel, R., Munro, Y., Nicol, J., Potthast, R., Rennie, M., Stein, T. H. M., Tanelli, S., Tridon, F., Walden, C. J., and Wolde, M.: WIVERN: A New Satellite Concept to Provide Global In-Cloud Winds, Precipitation, and Cloud Properties, Bulletin of the American Meteorological Society, 99, 1669–1687, https://doi.org/10.1175/BAMS-D-16-0047.1, 2018.

Imura, Y., Aoki, S., Kubota, T., Nakatsuka, H., Ohno, Y., and Okamoto, H.: Observation modes of EarthCARE/CPR with different Doppler measurement accuracy: Evaluation of their applicability, EGUsphere, 2026, 1–27, https://doi.org/10.5194/egusphere-2026-1453, 2026.

https://doi.org/10.5194/egusphere-2026-6816
Preprint. Discussion started: 17 November 2026
© Author(s) 2026. CC BY 4.0 License.

Japan Aerospace Exploration Agency (JAXA): EarthCARE/CPR L1B CPR one-sensor Received Echo Power Products and Doppler Product, https://www.doi.org/10.57746/EO.01jdvcydwjf63vpdbjp0vz6v64 (Accessed: 16 October 2026), 2024.

Japan Aerospace Exploration Agency (JAXA): EarthCARE/CPR Level 1b Product Definition Document, Tech. Rep. MAS-110009P, Japan Aerospace Exploration Agency (JAXA), 2025.

Kim, J., Kollias, P., Treserras, B. P., Battaglia, A., and Tan, I.: Evaluation of the EarthCARE Cloud Profiling Radar (CPR) Doppler velocity measurements using surface-based observations, EGUsphere, 2025, 1–21, https://doi.org/10.5194/egusphere-2025-2697, 2025.

Kim, J., Tan, I., Kollias, P., and Puigdomènech Treserra, B.: First EarthCARE CPR observations of dynamics–microphysics coupling in marine cold-Air outbreak clouds, Geophysical Research Letters, 53, e2025GL121 514, 2026.

Kollias, P., Tanelli, S., Battaglia, A., and Tatarevic, A.: Evaluation of EarthCARE Cloud Profiling Radar Doppler Velocity Measurements in Particle Sedimentation Regimes, Journal of Atmospheric and Oceanic Technology, 31, 366–386, https://doi.org/10.1175/JTECH-D-11-00202.1, 2014.

Kollias, P., Battaglia, A., Tatarevic, A., Lamer, K., Tridon, F., and Pfitzenmaier, L.: The EarthCARE cloud profiling radar (CPR) doppler measurements in deep convection: challenges, post-processing, and science applications, in: Remote Sensing of the Atmosphere, Clouds, and Precipitation VII, edited by Im, E. and Yang, S., vol. 10776, pp. 57 – 68, International Society for Optics and Photonics, SPIE, https://doi.org/10.1117/12.2324321, 2018.

Kollias, P., Battaglia, A., Lamer, K., Puigdomenech Treserras, B., and Braun, S. A.: Mind the Gap - Part 3: Doppler Velocity Measurements From Space, Frontiers in Remote Sensing, 3, https://doi.org/10.3389/frsen.2022.860284, 2022a.

Kollias, P., Puidgomènech Treserras, B., Battaglia, A., Borque, P., and Tatarevic, A.: Processing reflectivity and Doppler velocity from EarthCARE's cloud profiling radar: the C-FMR, C-CD and C-APC products, EGUsphere, 2022, 1–25, https://doi.org/10.5194/egusphere-2022-1284, 2022b.

Long, D. and Ulaby, F.: Microwave Radar and Radiometric Remote Sensing, Artech, 2015.

Manconi, F., Battaglia, A., and Kollias, P.: Characterization of surface clutter signal in the presence of orography for a spaceborne conically scanning W-band Doppler radar, Atmospheric Measurement Techniques, 18, 2295–2310, https://doi.org/10.5194/amt-18-2295-2025, 2025.

Markley, F. L. and Crassidis, J.: Fundamentals of Spacecraft Attitude Determination and Control, Springer New York, ISBN 978-1-4939-0802-8, https://doi.org/10.1007/978-1-4939-0802-8, 2014.

Puigdomènech Treserras, B., Kollias, P., Battaglia, A., Tanelli, S., and Nakatsuka, H.: EarthCARE's Cloud Profiling Radar Antenna Pointing Correction using Surface Doppler Measurements, EGUsphere, 2025, 1–16, https://doi.org/10.5194/egusphere-2025-1680, 2025.

Schutgens, N.: Simulating Range Oversampled Doppler Radar Profiles of Inhomogeneous Targets, Journal of Atmospheric and Oceanic Technology, 25, 1514–1528, 2008.

Sy, O. and Tanelli, S.: Recovering the Elusive Spectral Width From Spaceborne Doppler Profiling Radar Measurements: The "ExpliSyT" Approach, IEEE Transactions on Geoscience and Remote Sensing, 61, 1–23, 2023.

Tatarevic, A., Puigdomènech Treserras, B., and Kollias, P.: EarthCARE Product Definition Document (PDD): Product C-TC, Product Definition Document C-PRO_C-TC_PDD, Issue 11, Revision 6, McGill University, https://earthcarehandbook.earth.esa.int/documents/d/earthcare-data-handbook/earthcare-c-tc-level-2a-product-definition-document-pdd (Accessed: 22 October 2026), 2025.

Tatarevic, A., Puigdomènech Treserras, B., and Kollias, P.: EarthCARE Product Definition Document (PDD): Product C-FMR, Product Definition Document C-PRO_C-FMR_PDD, Issue 11, Revision 6, McGill University, https://earthcarehandbook.earth.esa.int/documents/d/earthcare-data-handbook/earthcare-c-fmr-level-2a-product-definition-document-pdd (Accessed: 22 October 2026), 2026.

https://doi.org/10.5194/egusphere-2026-6816
Preprint. Discussion started: 17 November 2026
© Author(s) 2026. CC BY 4.0 License.



Vallado, D. A. and McClain, W. D.: Fundamentals of Astrodynamics and Applications, vol. 21 of *Space Technology Library*, Microcosm Press, 4 edn., ISBN 978-1-881883-18-0, 2013.

Voosen, P.: NASA revives next-generation flagship Earth-observing missions, *Science*, https://www.science.org/content/article/nasa-revives-next-generation-flagship-earth-observing-missions (Accessed: 15 October 2026), 2026.

Walker McLinden, M. L., Li, L., M. Heymsfield, G. M., Coon, M., and Emory, A.: The NASA GSFC 94-GHz airborne solid-State Cloud Radar System (CRS), Journal of Atmospheric and Oceanic Technology, 38, 1001 – 1017, https://doi.org/10.1175/JTECH-D-20-0127.1, 2021.